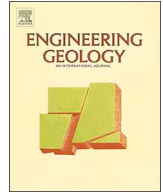




ELSEVIER

Contents lists available at ScienceDirect

## Engineering Geology

journal homepage: [www.elsevier.com/locate/enggeo](http://www.elsevier.com/locate/enggeo)

# Which fractures are imaged with Ground Penetrating Radar? Results from an experiment in the Äspö Hardrock Laboratory, Sweden

Justine Molron<sup>a,d,\*</sup>, Niklas Linde<sup>b</sup>, Ludovic Baron<sup>b</sup>, Jan-Olof Selroos<sup>c</sup>, Caroline Darcel<sup>a</sup>, Philippe Davy<sup>d</sup>

<sup>a</sup> Itasca Consultants S.A.S., 29 Avenue Joannès Masset, Lyon 69009, France

<sup>b</sup> Institut des sciences de la Terre, Université de Lausanne, Géopolis UNIL, Quartier Mouline, Lausanne 1015, Switzerland

<sup>c</sup> Swedish Nuclear Fuel and Waste Management Company (SKB), Evenemangsgatan 13, Box 3091, Solna SE-169 03, Sweden

<sup>d</sup> Univ Rennes, CNRS, Géosciences Rennes, UMR 6118, 263 Avenue Général Leclerc, Rennes 35042, France

## ARTICLE INFO

## Keywords:

Ground penetrating radar  
Surface-based method  
Fracture  
Core log  
Tunnel  
Statistical fracture model  
Nuclear waste disposal

## ABSTRACT

Identifying fractures in the subsurface is crucial for many geomechanical and hydrogeological applications. Here, we assess the ability of the Ground Penetrating Radar (GPR) method to image open fractures with sub-mm apertures in the context of future deep disposal of radioactive waste. GPR experiments were conducted in a tunnel located 410 m below sea level within the Äspö Hard Rock Laboratory (Sweden) using 3-D surface-based acquisitions (3.4 m × 19 m) with 160 MHz, 450 MHz and 750 MHz antennas. The nature of 17 identified GPR reflections was analyzed by means of three new boreholes (BH1-BH3; 9–9.5 m deep). Out of 21 injection and outflow tests in packed-off 1-m sections, only five provided responses above the detection threshold with the maximum transmissivity reaching  $7.0 \times 10^{-10} \text{ m}^2/\text{s}$ . Most GPR reflections are situated in these permeable regions and their characteristics agree well with core and Optical Televiewer data. A 3-D statistical fracture model deduced from fracture traces on neighboring tunnel walls show that the GPR data mainly identify fractures with dips between 0 and 25°. Since the GPR data are mostly sensitive to open fractures, we deduce that the surface GPR method can identify 80% of open sub-horizontal fractures. We also find that the scaling of GPR fractures in the range of 1–10 m<sup>2</sup> agrees well with the statistical model distribution indicating that fracture lengths are preserved by the GPR imaging (no measurement bias). Our results suggests that surface-GPR carries the resolution needed to identify the most permeable sub-horizontal fractures even in very low-permeability formations, thereby, suggesting that surface-GPR could play an important role in geotechnical workflows, for instance, for industrial-scale siting of waste canisters below tunnel floors in nuclear waste repositories.

## 1. Introduction

In hard rock systems, fractures are the main conduit for flow (Becker and Shapiro, 2000), for contaminant transport (Selroos et al., 2002), and they play a critical role in determining the mechanical properties of rocks (Davy et al., 2018a). Hydrogeological and geomechanical applications require, henceforth, an appropriate characterization of the fracture network and of its hydrological and mechanical properties (Davy et al., 2018a). Traditionally, this information is mostly derived from a statistical analysis of 2-D fracture traces mapped in tunnel walls and surface outcrops, or from 1-D fracture intercepts along boreholes. Such statistical approaches have drawbacks: 1) the 3-D fracture models do not rely on actual 3-D observations,

which requires crude assumptions on some fracture properties (e.g., fracture shapes) (Davy et al., 2018b); 2) some scales are hardly measured because of the limited size of outcrops, tunnel walls, or borehole diameter; 3) models that aim at making predictions are generally better constrained by conditioning to location-specific deterministic information than by global statistics only (Andersson and Dverstorp, 1987). This is why imaging fractures at different scales, especially with non-invasive methods, is of high importance for hydrogeological and geomechanical applications (e.g. mine and tunnel stability, detection of flow paths, contaminant transport).

A particular application, which partly motivates this study, is the detection of potential pathways (at the 10 m scale) from defective canisters for nuclear waste with non-invasive (i.e., without drilling)

\* Corresponding author.

E-mail addresses: [j.molron@itasca.fr](mailto:j.molron@itasca.fr) (J. Molron), [niklas.linde@unil.ch](mailto:niklas.linde@unil.ch) (N. Linde), [ludovic.baron@unil.ch](mailto:ludovic.baron@unil.ch) (L. Baron), [jan-olof.selroos@skb.se](mailto:jan-olof.selroos@skb.se) (J.-O. Selroos), [c.darcel@itasca.fr](mailto:c.darcel@itasca.fr) (C. Darcel), [philippe.davy@univ-rennes1.fr](mailto:philippe.davy@univ-rennes1.fr) (P. Davy).

<https://doi.org/10.1016/j.enggeo.2020.105674>

Received 4 December 2019; Received in revised form 5 May 2020; Accepted 7 May 2020

Available online 12 May 2020

0013-7952/ © 2020 The Authors. Published by Elsevier B.V. This is an open access article under the CC BY-NC-ND license (<http://creativecommons.org/licenses/by-nc-nd/4.0/>).

surface methods. This is required to identify locations that are unsuitable for storing nuclear waste in canisters emplaced under the tunnel floor, as envisioned for the storage of nuclear waste in Finland and Sweden. In the very low-permeability formations that are of interest for the nuclear waste repositories of Sweden or Finland, transport of potentially released radionuclides take place through fractures with sub-millimetric apertures that are very difficult to detect remotely. This excludes many geophysical methods such as seismic reflection/refraction, electrical resistivity and nuclear magnetic resonance for this task. If one adds both the constraint of being surface-based and being able to detect meter-scale individual fractures remotely, the only suitable method is ground penetrating radar (GPR) (Day-Lewis et al., 2017).

There is a rich literature describing how GPR data were used to detect permeable fractures in various hydrogeological (Becker and Tsoflias, 2010; Day-Lewis et al., 2003; Dorn et al., 2011a; Dorn et al., 2011b; Dorn et al., 2012; Shakas et al., 2016; Tsoflias et al., 2001), geotechnical (Davis and Annan, 1989; Grasmueck et al., 2005a; Grégoire and Halleux, 2002; Seol et al., 2001) and nuclear waste-related (Baek et al., 2017; Döse and Carlsten, 2017; Olsson et al., 1992; Serzu et al., 2004) applications. Notably, the GPR reflections caused by fracture planes are enhanced when the fractures are fluid-filled or have large apertures (Grasmueck, 1996; Hollender and Tillard, 1998; Hollender et al., 1999; Jeannin et al., 2006; Markovaara-Koivisto et al., 2014; Shakas and Linde, 2017; Tsoflias and Becker, 2008; Tsoflias and Hoch, 2006). Electromagnetic (EM) waves with wavelengths on the m-scale respond to fractures with sub-millimetric aperture because of the strong contrast in electrical properties between the fracture filling and the surrounding rock matrix and because of multiple internal reflections between the fracture walls generating wavelet interferences (the thin-bed response) (Bradford and Deeds, 2006; Deparis and Garambois, 2008; Grégoire and Hollender, 2004; Sassen and Everett, 2009; Shakas and Linde, 2015). At repository depth (~400–600 m below sea level), the fracture aperture can be very small and it is not yet clear whether observed GPR reflections in such an environment are primarily related to water-filled fractures and not to other geological interfaces (e.g., dike intrusion, geological contacts, material-filled fractures). It is also not clear which percentage of open fractures are imaged as a function of their sizes and orientations.

In this contribution, we present a 3-D GPR imaging experiment performed at 410 m depth in the Äspö Hard Rock Laboratory, Sweden (Fig. 1a). The GPR data have been migrated to form a 3-D network of reflectors, hereafter, named GPR fractures. After the GPR experiment, three 9-m deep boreholes were drilled in the zone (Fig. 1b), mapped with televiewer logging, and hydraulically tested to ground-truth the GPR results.

Our main aims are to address the following questions:

1. Do GPR reflections observed in deep low-permeability granitic formations correspond to open transmissive fractures only or also to other types of geological discontinuities?
2. What is the detection accuracy of the GPR fractures in terms of fracture sizes and orientations?

The first point has been addressed by a careful GPR experiment performed in a 410-m deep tunnel by picking the main reflectors and verifying the nature of reflectors from a subsequent drilling of three boreholes analyzed by core logging and hydraulic tests. The second point has been addressed by comparing the statistics of GPR fractures with the 3-D fracture statistics derived from outcrop and borehole mapping.

## 2. Test Site

The Äspö Hard Rock Laboratory (HRL) is an underground research facility below the island of Äspö located approximately 300 km south of Stockholm on the peninsula of Simpevarp surrounded by the Baltic Sea

(Fig. 1a). It was constructed in 1986 (Cosma et al., 2001) by the Swedish Nuclear Fuel and Waste Management Company (SKB) as a R&D site to develop new methodologies and technologies to build the know-how needed to construct a hard rock repository for nuclear waste. It contains a main tunnel of 3.6 km length and several side-tunnels extending from the surface down to 450 m depth (Fig. 1a) (SKB, 2016). The geology is mainly composed of fractured granitic rocks that are more than 1.7 billion years old (Cosma et al., 2001).

The GPR investigation focuses on the secondary TAS04 tunnel, which was excavated at a depth of 410 m by the drill-and-blast method (Ericsson et al., 2015; Ericsson et al., 2018). The tunnel is 36 m long, 4.2 m wide and 5.3 m high. Its geology is composed by three main rock types: fine-grained granite, Äspö diorite and Ävrö granodiorite, with some pegmatite veins (Fig. 1b) (Ericsson et al., 2015; Ericsson et al., 2018). Geotechnical (check of drilling and charging), geological (fracture mapping), geophysical (surface GPR) and hydrogeological (42 borehole drillings of 2 m depth and hydraulic tests) investigations were used to characterize superficial fractures induced by the blasting. It was found that the excavation-damage zone (EDZ) was 0.5 m thick (Ericsson et al., 2015; Ericsson et al., 2018). The EDZ was removed by cutting and sawing the tunnel floor with a diamond wire along 20 m of the tunnel length; it is in the resulting very flat area that our GPR measurements were performed (Fig. 1b).

In addition to the TAS04 tunnel, three surrounding tunnels at the same depth are used to derive the 3-D statistical fracture model. The TAS05 and TASN tunnels are parallel to the TAS04 and are 17 m and 52 m long, 4.5 m and 4.2 m wide and 4.5 m and 3.7 m high, respectively. The TASP tunnel is perpendicular to the others and is 57 m long, 7 m wide and 4.1 m high.

## 3. GPR experiment methodology

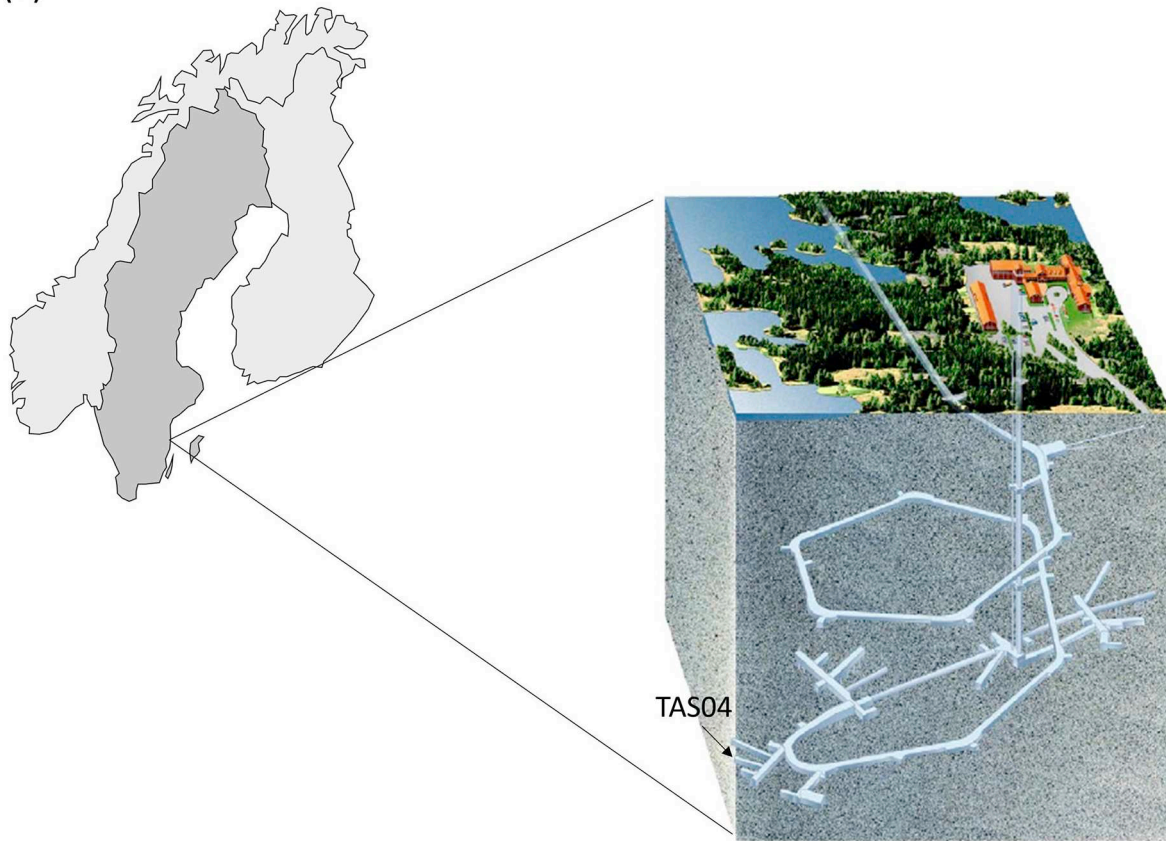
### 3.1. GPR survey

The GPR data from the TAS04 tunnel were acquired in the period of November 6–10, 2017, using the MALÅ GroundExplorer (GX) HDR-serie (High Dynamic Range), equipped with skid plate and wheel. 160, 450 and 750 MHz antennas were used to achieve different investigation depths and image resolutions. The acquisition parameters are given in Table 1. The shielded transmitter and receiver antennas, separated by a fixed separation in a so-called common-offset configuration (Annan, 2003), were pulled along the cleaned and flat tunnel floor (Fig. 2). The GPR profiles were acquired with 2.34 cm measurement spacing and a line separation of 0.05 m for the 450 and 750 MHz surveys and 0.10 m for the 160 MHz survey. The profiles were oriented along the tunnel length (x-direction) using multiple orthogonal measurement tapes to ensure straight and parallel measurement lines. The resulting acquisition area was 3.4 m × 19 m. Measurements with a total station using fixed geodetic points in the tunnel were used to convert the acquisition geometry into the local Äspö coordinate system (Äspö96).

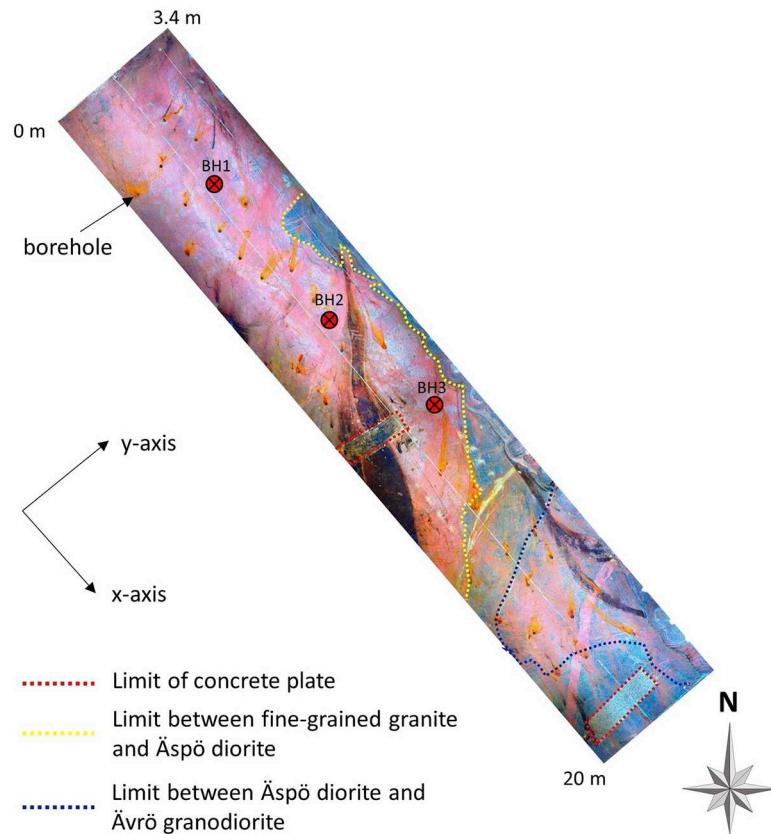
### 3.2. Data processing

The GPR data processing and migration workflow is depicted in Fig. 3. We consciously avoid automatic gain control to enable relative comparisons of reflectivity at different locations in the investigated volume. The editing step involves removal of some limited data at the end of certain profiles to ensure a rectangular-shaped survey area. Direct Current (DC) removal used to remove offsets in the data is achieved by subtracting the mean of the last 33% of the GPR traces. Time zero corrections are made to ensure that the actual source initiation time is treated as zero. For each trace, this is achieved by shifting the time vector such that the time when the signal magnitude is first above the noise-level corresponds to the time it takes for the speed of light in a vacuum to travel the distance between the source and receiver. Irregularity removal refers to traces that are adversely affected by the many

(a)



(b)



(caption on next page)

**Fig. 1.** (a) Illustration of the Äspö Hard Rock Laboratory in the Simpevarp peninsula, Sweden. The study tunnel (TAS04) is situated at a depth of 410 m. Figure modified from SKB (2016), courtesy of SKB, Illustrator: Jan Rojmar. (b) Orthophotography of the tunnel floor showing the geological limit between fine-grained granite (to the left), Äspö diorite and Ävrö granodiorite (to the right) indicated by yellow and blue dashed lines, shallow pre-existing boreholes represented by black dots with oxidation (orange traces) and concrete plates delimited by red dashed lines. The three new boreholes (BH1, BH2 and BH3 indicated by red circles with crosses) were drilled in the granitic formation with locations chosen based on the GPR results. (For interpretation of the references to colour in this figure legend, the reader is referred to the web version of this article.)

**Table 1**  
Experimental parameters used for the 3-D GPR acquisitions in common-offset mode.

Parameters	Frequencies (MHz)		
	160	450	750
Antenna separation (m)	0.33	0.18	0.14
Measurement spacing (m)	0.02355	0.02355	0.02355
Profile separation (m)	0.10	0.05	0.05
Number of profiles	34	69	69
Investigation depth (m)	0 to 10	0 to 8	0 to 5

(42) shallow boreholes (0–1 m depth) and two concrete plates. To avoid the migration of these data that largely respond to non-geologic features, we automatically detected (5–6% of the data) and removed these traces by identifying irregularities in the magnitudes of their direct waves. Median trace removal along each line was performed to not only remove the direct wave, but also significant ringing in the data. Time-gain with a different exponent for each frequency (2.5 for 160 MHz, 2.5 for 450 MHz and 2.0 for 750 MHz data) was applied to correct for geometric spreading and attenuation of later-arriving signals. Finally, singular value decomposition (SVD) was used to remove the first 3 to 5 singular values to further suppress ringing effects.

Migration was needed to collapse the many diffractors in the data and to properly locate the reflections at depth. For this, we used 3-D depth Kirchhoff migration (Margrave and Lamoureaux, 2019) as implemented in the CREWES Matlab toolbox (CREWES, 1988) with a constant velocity of 0.130 m/ns as determined by diffraction analysis and visual inspection of migration results.

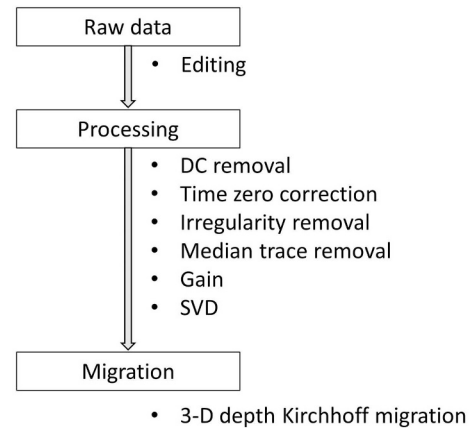


**Fig. 3.** Flow chart describing how the raw data are edited and processed before migration.

**4. Results**

The 3-D GPR results are exemplified by processed profiles of 160 MHz (Fig. 4), 450 MHz (Fig. 5) and 750 MHz (Fig. 6) data and corresponding 3-D migration results along a 2-D section located approximately in the middle of the tunnel. As expected, the 750 MHz data have the highest resolution and the lowest investigation depth, while the 160 MHz data have the lowest resolution and the highest investigation depth. The 450 MHz is the most suitable frequency for identifying each individual feature from 0 to 8 m depth. To a first order, the vertical and horizontal resolution enabling separation of features in

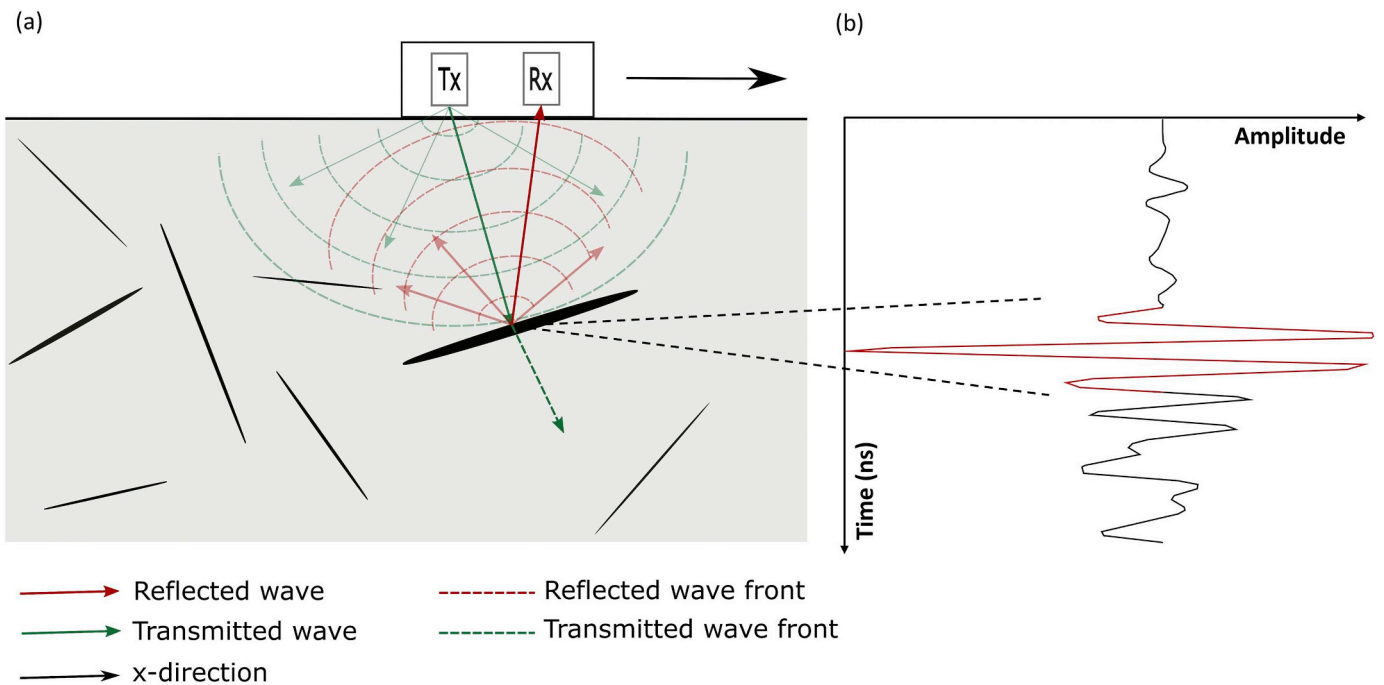


**Fig. 2.** (a) The common-offset GPR configuration: the transmitter (Tx) and receiver (Rx) antennas are placed in a shielded box. The surface GPR is pulled along the tunnel floor (x-direction). The transmitter antenna sends an electromagnetic pulse into the subsurface and the receiver antenna records the returning signal amplitudes over time as shown schematically in (b).

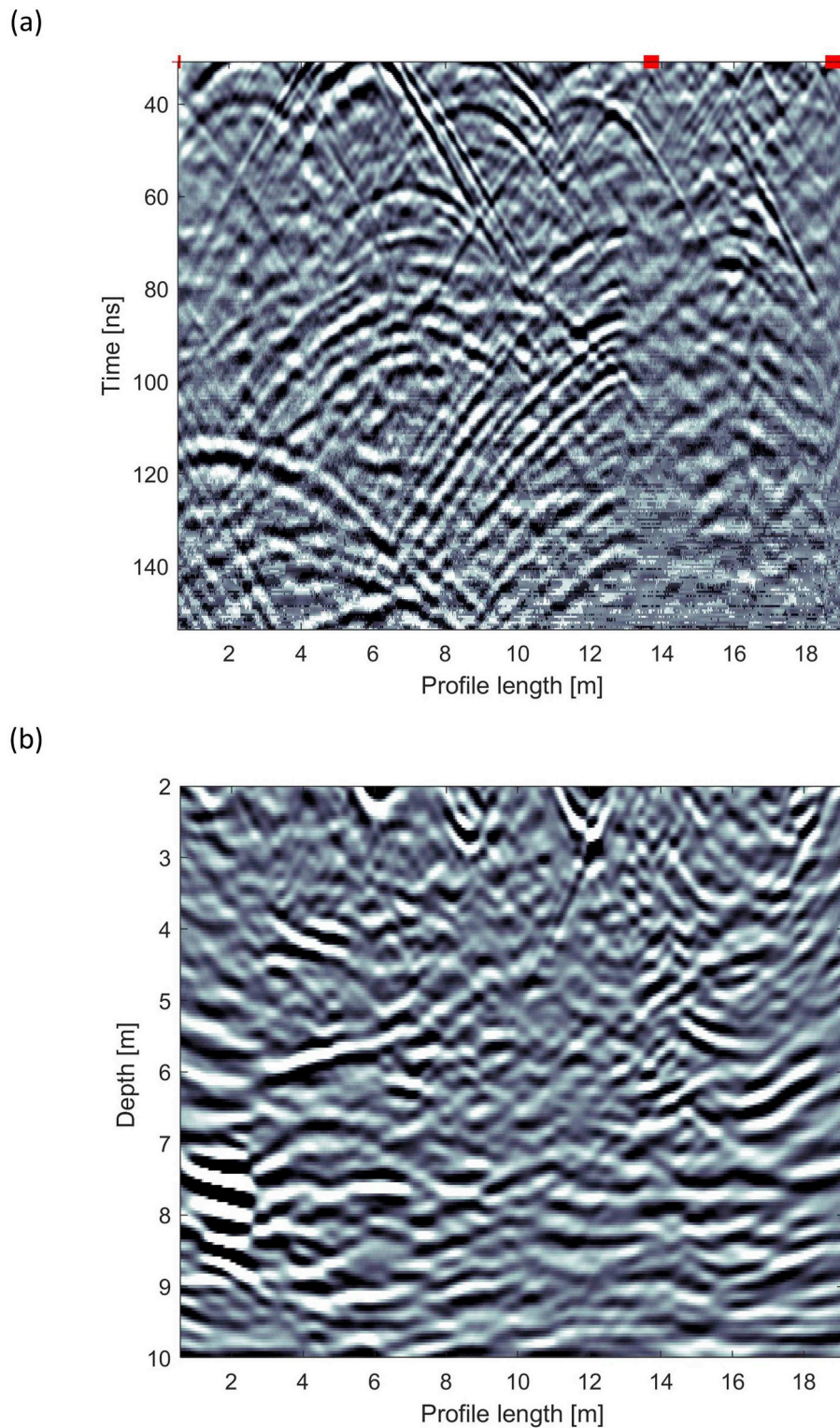


**Fig. 4.** (a) Processed 2-D GPR slice acquired with 160 MHz antennas at  $y = 2.25$  m. Red plus signs correspond to shallow boreholes and concrete plate irregularities; the corresponding traces are removed before migration. (b) Migrated data based on 3-D Kirchhoff migration with a constant velocity of 0.13 m/ns. The time and depth intervals are chosen based on the associated resolution and depth of penetration. (For interpretation of the references to colour in this figure legend, the reader is referred to the web version of this article.)

migrated images are  $\lambda/4$ , where  $\lambda$  is the wavelength (Annan, 2003; Grasmueck et al., 2005b; Jol, 2008; Reynolds, 1997). Since the average wave speed is 0.13 m/ns, the vertical and horizontal resolutions are 0.2 m for 160 MHz, 0.06 m for 450 MHz and 0.04 m for 750 MHz.

The unmigrated data (Fig. 4a, Fig. 5a, Fig. 6a) show diffractions

manifested by characteristic hyperbolas. The shallow diffractions are mainly caused by the shallow boreholes (42), while deeper diffractions may be related to fracture wall irregularities, fracture intersections or geological heterogeneities (Grasmueck et al., 2015; Grasmueck et al., 2013; Grasmueck et al., 2005a). On depth slices, these diffractions

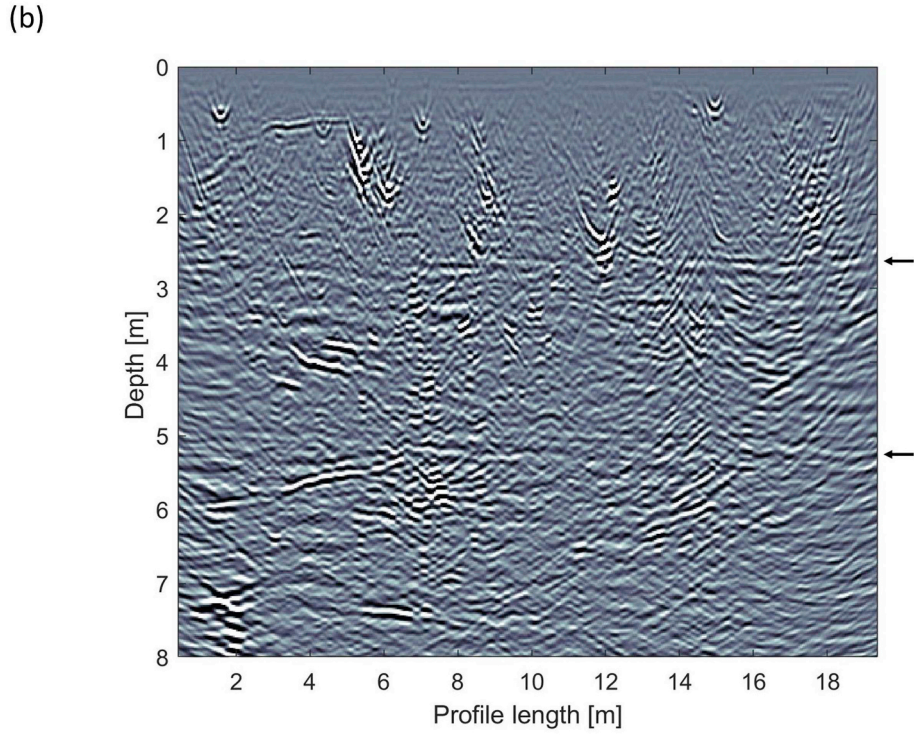
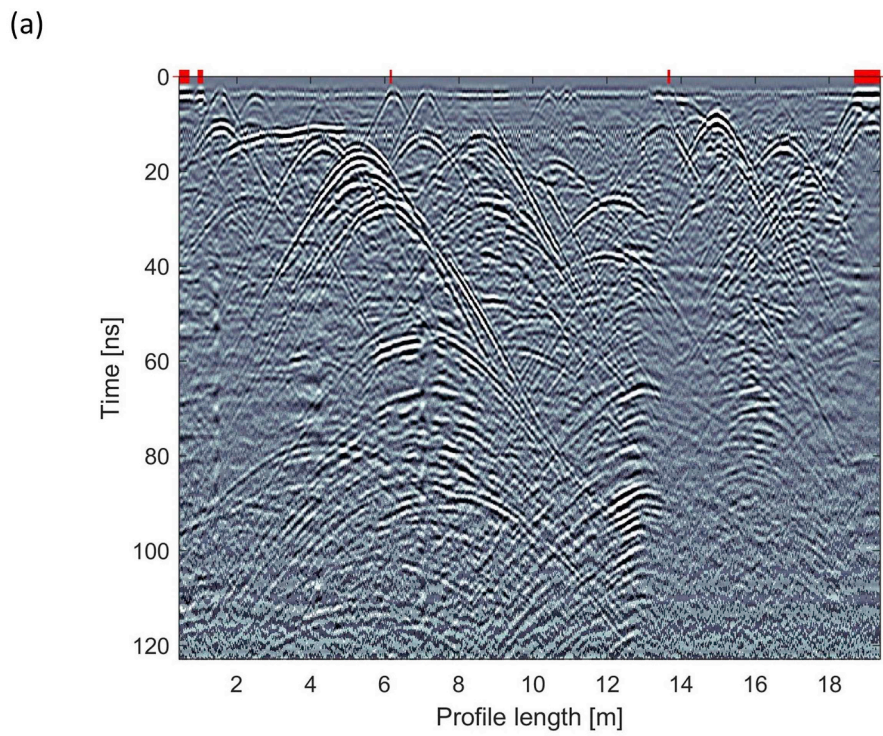


**Fig. 5.** (a) Processed 2-D GPR slice acquired with 450 MHz antennas at  $y = 2.28$  m. Red plus signs correspond to shallow boreholes and concrete plate irregularities; the corresponding traces are removed before migration. (b) Migrated data based on 3-D Kirchhoff migration with a constant velocity of 0.13 m/ns. The depth interval is chosen based on the associated resolution and depth of penetration. The large horizontal features at depths of 2.5 and 5.1 m (indicated by black horizontal arrows) are attributed to reflections at the tunnel roof and corresponding multiples. (For interpretation of the references to colour in this figure legend, the reader is referred to the web version of this article.)

appear as concentric circles, whose radii are increasing with depth (Fig. 7a).

To remove the diffractions and locate the reflections in space, we used 3-D Kirchhoff migration with a constant velocity of 0.13 m/ns. After migration, the energy contained in the hyperbola tails is ideally gathered into a unique point corresponding to the initial diffraction point (Fig. 7b). After migration, sub-horizontal reflections that might correspond to fractures are visible on vertical 2-D GPR slices with

alternating positive and negative amplitudes aligned in sub-horizontal patterns (Fig. 4b, Fig. 5b, Fig. 6b). This alternation is a consequence of the finite-length source wavelet used by the GPR antennas. Sub-vertical features that might correspond to fractures appear as bright spots plunging with depth that are clearly visible in the horizontal GPR depth slices (Fig. 7b, c).

To visualize the GPR results in three dimensions, we imported 2-D processed and migrated data slices into the software Paradigm

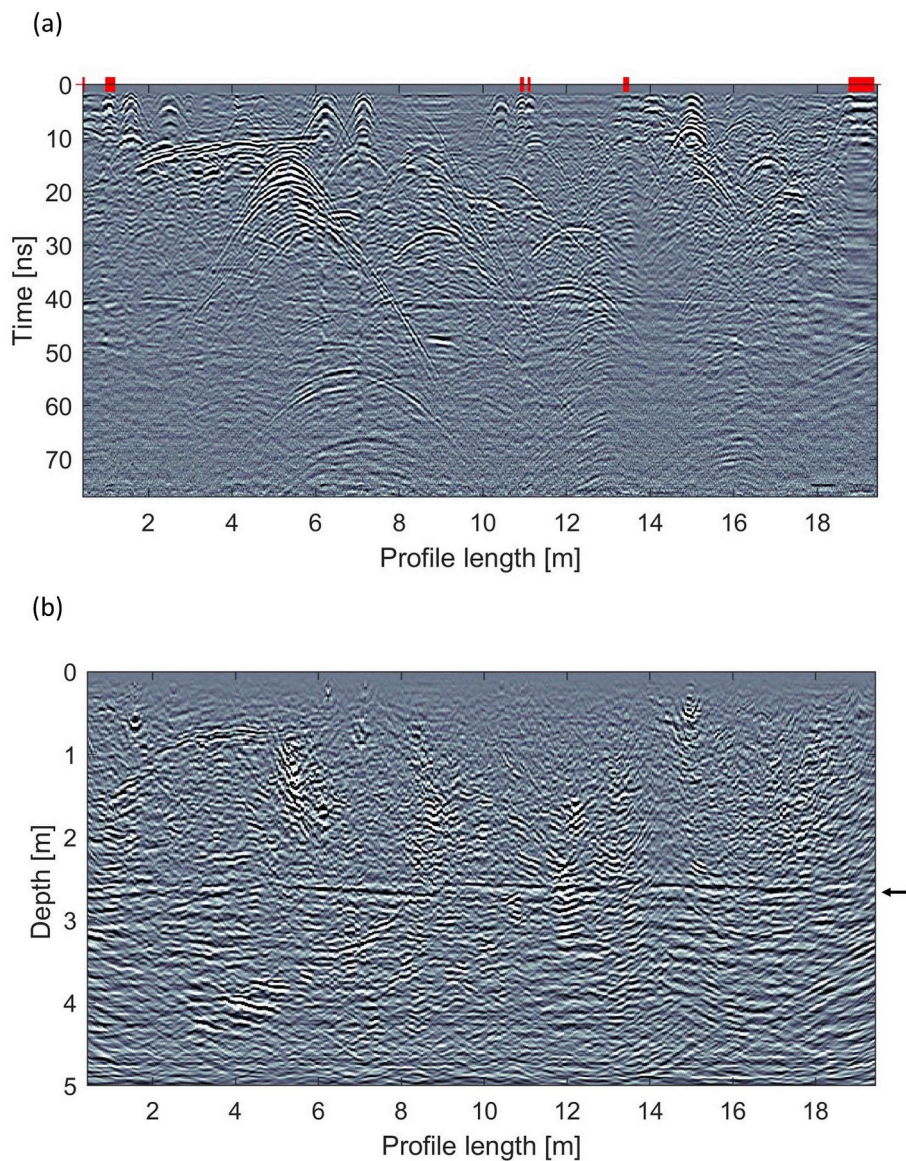


**Fig. 6.** (a) Processed 2-D GPR slice acquired with 750 MHz antenna at  $y = 2.28$  m. Red plus signs correspond to shallow boreholes and concrete plate irregularities; the corresponding traces are removed before migration. (b) Migrated data based on 3-D Kirchhoff migration with a constant velocity of 0.13 m/ns. The depth interval is chosen based on the associated resolution and depth of penetration. The large horizontal feature at a depth of 2.5 m (indicated by a black horizontal arrow) is attributed to reflections at the tunnel roof. (For interpretation of the references to colour in this figure legend, the reader is referred to the web version of this article.)

GOCAD™ (Fig. 8) using Äspö coordinates. By comparing unmigrated (Fig. 4a, Fig. 5a, Fig. 6a) and migrated (Fig. 4b, Fig. 5b, Fig. 6b) data for the three frequencies, we created a simplified fracture network model (Fig. 8). This manual procedure of identifying GPR fractures is somewhat subjective. Large sub-horizontal GPR structures were picked on each vertical 2-D slice at the interface between the background signal and the signal corresponding to the reflection of the structure represented by positive (intense white) or negative (intense black) amplitudes. Sub-vertical fractures were identified on horizontal depth slices by picking their horizontal edge traces (Fig. 7c). The set of the trace picks was used to construct the fracture surface using the convex hull plane that connects the picks, with no assumption on fracture form

in order to avoid over- or underestimation of the data. We identified a total of 21 reflections that might correspond to fractures with dimensions of 1 to 4 m. This work was focused on the first 15 m of the GPR block along the axis of the tunnel, in order to be within the same fine-grained granitic environment (Fig. 8).

### 5. Verification of GPR fractures with borehole data

Based on our simplified GPR fracture model, we sited three boreholes of 9.0 to 9.5 m depth with a diameter of 0.076 m: BH1 (K04018G02) in a region with multiple sub-horizontal reflections that we expected would correspond to an overall more transmissive region,

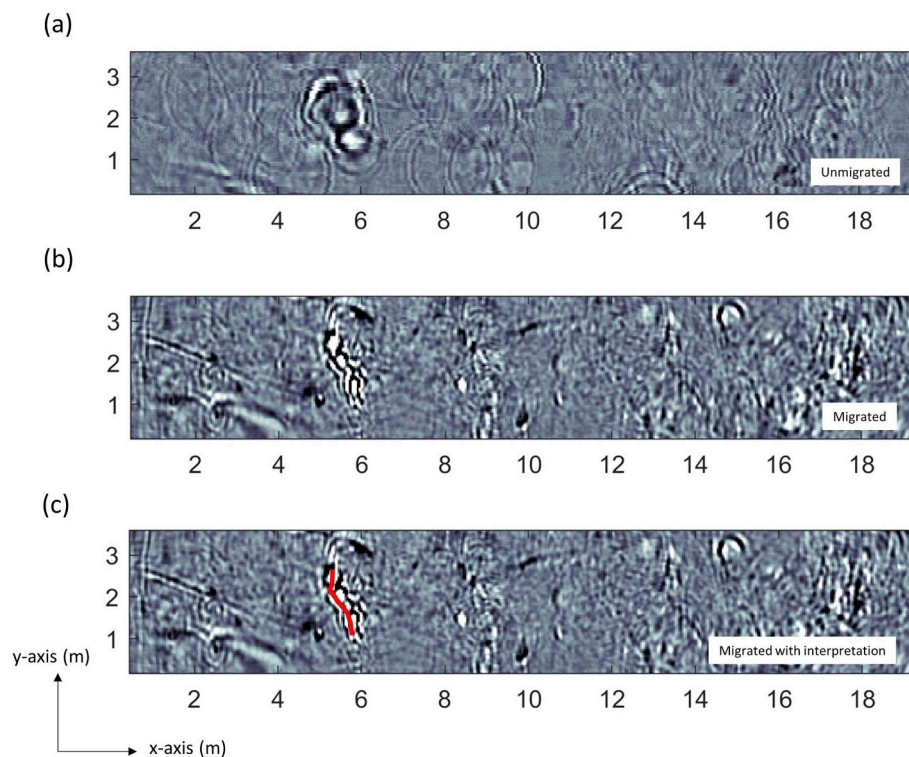


Fig. 7. Depth slices obtained from 450 MHz data at 1.32 m depth illustrating diffractions that are likely due to sub-vertical fractures. (a) Unmigrated processed data for which the diffractions are represented by circular shapes. (b) Migrated data in which the diffractions collapse and (c) the corresponding sub-vertical features can be identified manually.

BH2 (K04022G02) in a region of prominent sub-vertical reflections and diffractions with an expected significant transmissivity and BH3 (K04026G02) in a region with few GPR reflections suggesting that it would contain fewer open fractures and be less permeable than BH1 and BH2 (Fig. 8). Because of technical constraints, the boreholes had to be separated by at least 3 m and located at a certain distance away from the 42 shallow pre-existing boreholes and concrete plates. The final locations of the boreholes are seen in Fig. 1b.

After drilling, BH1 was sealed and its pressure was monitored during the drilling of BH2 and BH3. The same procedure was followed for BH2 during the drilling of BH3. This provides useful information about the hydraulic connections between boreholes. All boreholes were cored and imaged with a televiewer in order to map intersecting fractures. The orientation and openness of the intersecting fractures were subsequently determined from these data.

### 5.1. Connectivity between boreholes

During the drilling of BH2, the pressure in BH1 showed two periods of net decreases (Fig. 9a) corresponding to the boring of sections from 3.2 to 3.5 m depth and from 7.1 to 7.5 m depth. This suggests that BH1 is at least connected to fractures at these two section depths in BH2. During the drilling of BH3, pressure in BH1 (not shown) and BH2 (Fig. 9b) showed similar behavior with three distinct decreases corresponding to the boring of BH3 in the sections from 1.9 to 2.9 m, 4.9 to 5.2 m and 6.4 to 6.9 m depth, respectively. Due to the vicinity to BH3, the pressure drop in BH2 is three times higher than in BH1. Finally, the stationary pressure (1850 kPa in BH1, 2050 kPa in BH2 and 2150 kPa in BH3) in each packed-off borehole indicates a strong hydraulic gradient from BH3 towards BH1.

### 5.2. Hydraulic tests

The hydraulic properties of the fractured rock were estimated from injection and outflow tests in 1-m packed-off sections from 1 to 8 m depth (Andersson and Ragvald, 2019) by means of a High pressure Water Injection Controller (HWIC) equipment (Hjerne et al., 2013) that automatically measures the injection or outflow with a constant imposed pressure. Most of the tests (Table 2) were performed with outflowing conditions due to the very high ambient borehole pressure (approximately 2000 kPa). In some sections, the pressure could not return to its initial state quickly enough after an outflow test and injection tests were performed.

Of the 21 1-m sections being tested, only 5 sections (3 for BH1, 1 for BH2 and 1 for BH3) provided a flow rate above the measuring limit of the flowmeter (2 mL/min). Hydraulic transmissivities of the 1-m sections were then estimated by Andersson and Ragvald (2019) using Moye's formula (Moye, 1967) assuming that steady-state was reached at the end of each test:

$$T_M = Q_p \cdot \rho_w \cdot g \cdot C_M / dP_p, \tag{1}$$

$$C_M = (1 + \ln(L_W / 2r_w)) / 2\pi, \tag{2}$$

where  $T_M$  is the hydraulic transmissivity ( $m^2/s$ );  $Q_p$  is the flow rate at the end of the flow duration ( $m^3/s$ );  $\rho_w$  is the water density ( $kg/m^3$ );  $g$  is the acceleration of gravity ( $m/s^2$ );  $C_M$  is the geometrical shape factor;  $dP_p$  is the injection/outflow pressure differences;  $L_W$  is the measurement section length and  $r_w$  is the borehole radius (m). Based on the results (Table 2), the rock is found to have a very low transmissivity with the five 1-m sections above the detection limit having transmissivities ranging between  $2.2$  and  $7.0 \times 10^{-10} m^2/s$ .

The boreholes with the transmissive zones highlighted are plotted

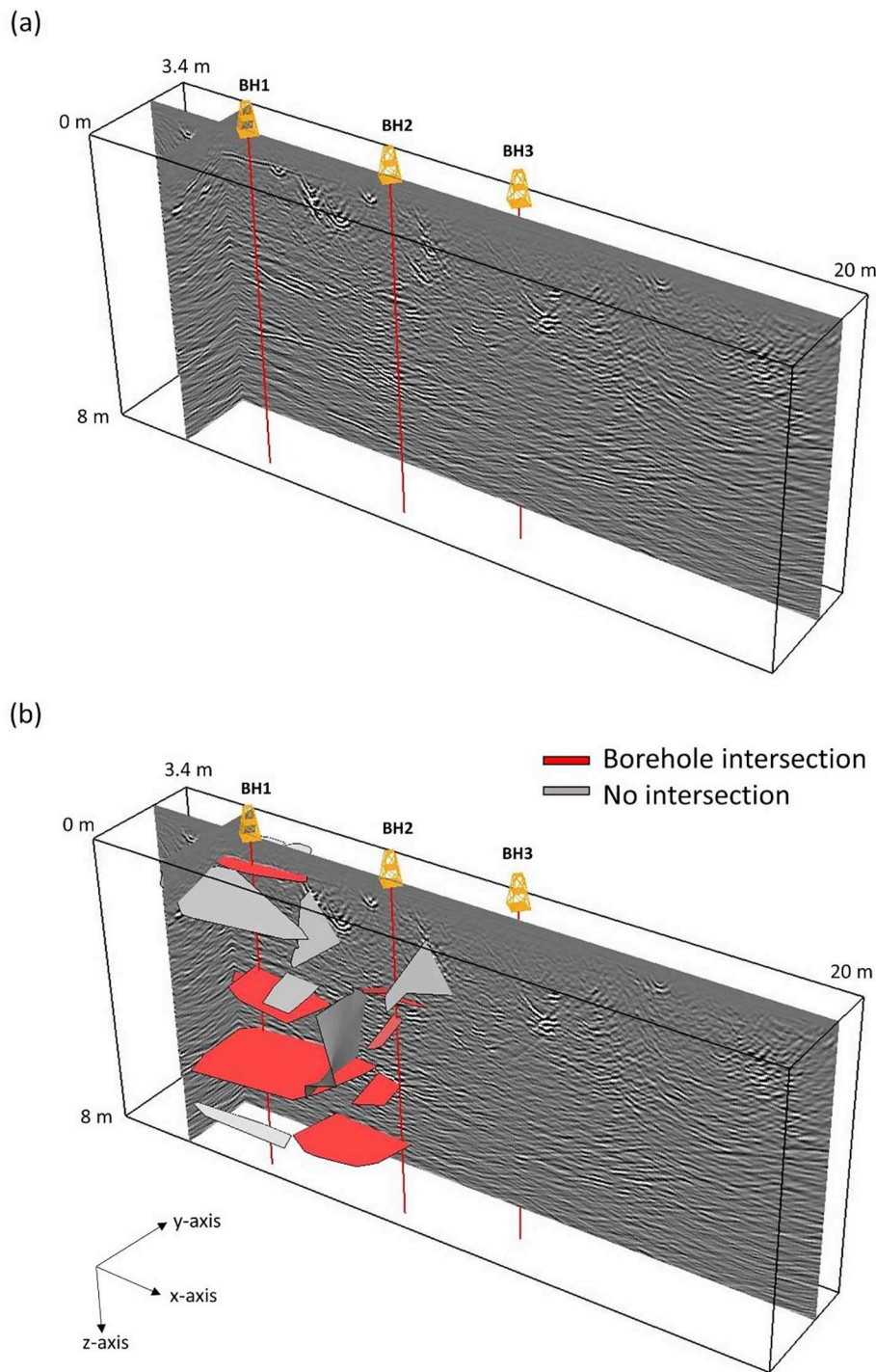


**Fig. 8.** Fence diagrams displaying the migrated 450 MHz data. (a) The migrated GPR data based on which three boreholes (BH1, BH2 and BH3) were drilled. The basis for the borehole design is illustrated in (b) where GPR reflections corresponding to expected fractures are displayed. The strong reflections were manually picked at the interface between the background signal and the signal corresponding to the reflection of the structure. The fracture planes were constructed by the convex hull method and the fractures intersecting the boreholes are represented in red. Reflections are only interpreted in the region of fine-grained granite (first 15 m). (For interpretation of the references to colour in this figure legend, the reader is referred to the web version of this article.)

together with crossing migrated 450 MHz GPR slices in Fig. 10. Strong and large sub-horizontal reflections traversing the boreholes are highlighted. Four such reflections are identified near BH1 with three of them being situated in the transmissive zone. Along BH2, six strong (but not very large) reflectors are identified with two being situated in the transmissive zone. No strong reflectors are identified along BH3.

### 5.3. Fracture mapping

Fracture characteristics (e.g., position, depth, strike, dip, filling mineralogy, open/sealed information) were obtained by Optical Televiwer (OPTV) and core logging (Andersson and Ragvald, 2019). With the position and orientation information, we could implement the

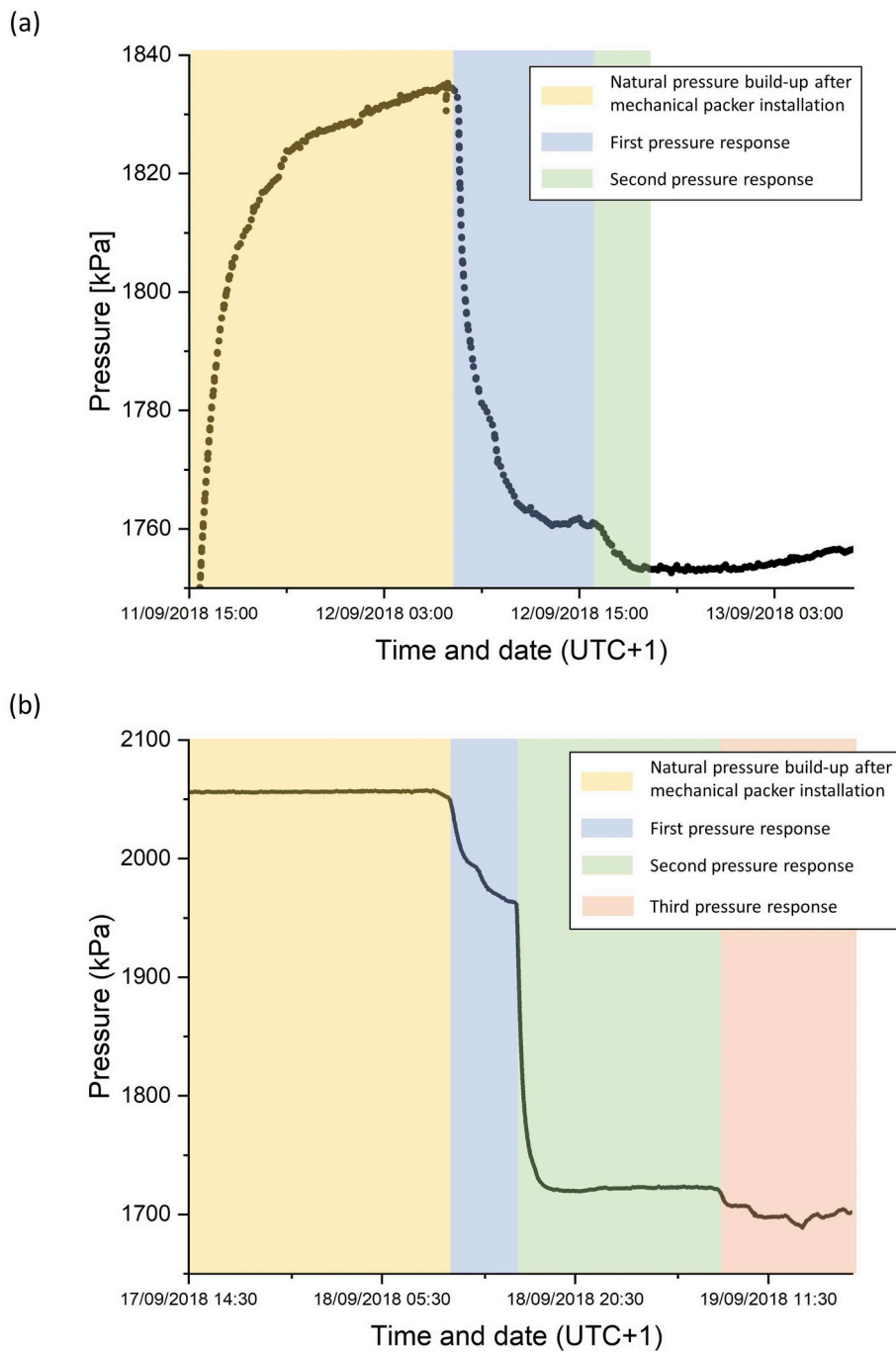


Fig. 9. Pressure responses observed in observation boreholes while drilling new boreholes. Pressure response in (a) BH1 during the drilling of BH2 and (b) BH2 during the drilling of BH3. The first part of the curves (yellow) represents pressure rise due to the installation of a mechanical packer in drilled borehole at 1 m depth. The initiations of pressure drops (blue, green and orange) correspond to drilling of borehole sections (3.2–3.5 m and 7.1–7.5 m in BH2 and 1.9–2.2, 4.9–5.2 m and 6.4 m in BH3). A subsequent smaller pressure decrease is also observed in BH2 (blue part) corresponding to the drilling between 2.7 and 2.9 m in BH3. (For interpretation of the references to colour in this figure legend, the reader is referred to the web version of this article.)

fractures into our database, describing the fractures as disks centered on the boreholes. This enables a detailed assessment of the agreement between the GPR reflections and the fractures seen in the core logging (Fig. 11, Fig. 12, Fig. 13).

We present the fracture positions in terms of depth, orientation (strike and dip) and opening (sealed or open) using tadpole plots (Fig. 11a, Fig. 12a and Fig. 13a). This interpretation is based on

televviewer and core inspection in the laboratory. Each borehole is represented by a cylinder divided into 1-m sections used for hydraulic measurements with indication of GPR reflections crossing the borehole and the sections with recorded outflows above the measurements limit (Fig. 11b, Fig. 12b and Fig. 13b). Fence diagrams are used to highlight strong GPR reflections along the boreholes and to compare them with fractures seen on cores (Fig. 11c,d, Fig. 12c,d and Fig. 13c). To do so,

**Table 2**

Results of hydraulic tests in 1-m packed-off sections for each borehole (BH1 to BH3) using High pressure Water Injection Controller (HWIC) equipment (Hjerne et al., 2013). Pressure measured in each 1-m test section shows the variation due to the hydraulic disturbance: injection tests give positive pressures and outflow tests give negative pressures. Hydraulic transmissivity was calculated from Moye's formula (Moye, 1967).

Borehole ID	Test section (m)	Pressure (kPa)	Flow rate (L/min)	Hydraulic transmissivity (m <sup>2</sup> /s)
BH1	1–2	200	< detection limit	
	2–3	510	< detection limit	
	3–4	–1427	–0.0033	2.2E-10
	4–5	–1086	–0.0073	6.3E-10
	5–6	–1080	–0.0065	5.6E-10
	6–7	–1449	< detection limit	
	7–8	–1376	< detection limit	
	BH2	1–2	656	< detection limit
2–3	–1875	< detection limit		
3–4	–1589	–0.0038	2.2E-10	
4–5	400	< detection limit		
5–6	–1979	< detection limit		
6–7	–1600	< detection limit		
7–8	–1979	< detection limit		
BH3	1–2	175	< detection limit	
	2–3	–833	< detection limit	
	3–4	191	< detection limit	
	4–5	–1300	–0.0097	7.0E-10
	5–6	–1600	< detection limit	
	6–7	–1659	< detection limit	
	7–8	–1300	< detection limit	

we superimposed fractures from core log data on the GPR sections crossing the borehole, and observed the match based on fracture depth, strike and dip. We assume that a GPR fracture matches a fracture intersection trace if their depth and dip do not exceed a deviation of 0.3 m and 15°, respectively (Table 3). The strike is also used to assess the fracture matching, but its uncertainty is particularly high for sub-horizontal fractures. Consequently, we used a maximum strike deviation of 60°. The corresponding fracture intercepts are well seen in the OPTV images (Fig. 11e,f, Fig. 12e,f and Fig. 13d).

Along BH1 (Fig. 11), we observed four strong reflections that match very well with four fractures seen on cores. The maximum disagreement in terms of fracture depth, dip and strike are 0.1 m, 6° and 54°, respectively (Table 3). The fractures have all been interpreted as open and three of them are located in the transmissive region (above the flow measurement threshold) while the remaining fracture is located in the 0 to 1 m interval where no hydraulic tests were made. We note that this corresponds to a rather ideal case for GPR data, as the identified transmissive fractures all have low dips for which the GPR reflections are the strongest.

Along BH2 (Fig. 12), five reflections have been identified (Fig. 10) that are generally less strong than those crossing BH1. Since the fractures observed in this borehole are mostly composed by sub-vertical fractures (75%), the surface GPR data contain multiple diffractions (Fig. 5) that clutter the resulting migrated images and make the match with any sub-horizontal fractures non-trivial. This superposition of energy is particularly present in the area situated between 2.8 and 3.8 m. The two first reflections seem to match with two sets of closely separated sub-horizontal fractures that are interpreted as open. Each set is composed by two fractures separated by 0.1 m. The first set is well correlated in terms of depth, dip and strike with the first reflector. The second set is well correlated in terms of depth and strike with the second reflector while the dip is above the threshold. The third

reflection matches well in terms of depth, dip and strike with a fracture at 3.7 m of depth (Table 3). These five open fractures are concentrated in the zone where flow could be measured (the first fracture is situated at 0.1 m above this measured section). The strong reflector that appears to cross the borehole at 5.7 m depth does not correspond to any borehole fractures. Such a mismatch can be explained by the fact that borehole data give punctual information while GPR gives a measure that is averaged on a roughly metric scale. This implies that the geological heterogeneity or fracture corresponding to this reflection could be next to the borehole. The last reflector, matching in terms of depth, strike and dip with an open fracture at 7.4 m, is located in the borehole section (7.13 to 7.54 m) that produced a pressure response in BH1 during the drilling of BH2. Even if its transmissivity could not be determined because of the flowmeter threshold, it does provide a strong GPR reflection. This suggests that this fracture is locally less permeable at the borehole location, which is also indicated by the GPR reflectivity that is significantly increased away from the borehole.

BH3 is mostly composed by sub-vertical (90%) and sealed (80%) fractures that highly limit the possibility of imaging fractures with the surface GPR method. In the transmissive region, all open fractures have dips exceeding 60°. Consequently, no GPR fracture was identified (Figs. 10, 13).

The match between GPR data and borehole data (pressure, hydraulic and core logging data), for BH1 and BH2, shows that fractures interpreted by GPR are mostly situated in the most transmissive hydraulic sections measured along boreholes. Most remaining GPR reflections showed correlation with depth sections being connected to other boreholes (pressure measurements) or matched with fractures from borehole (core log data). In one case, it had to be assumed that the fracture was positioned just next to the borehole. The reason that no fracture is seen by GPR along BH3, despite that it contains the most permeable 1-m section, is explained by the significant number of sub-

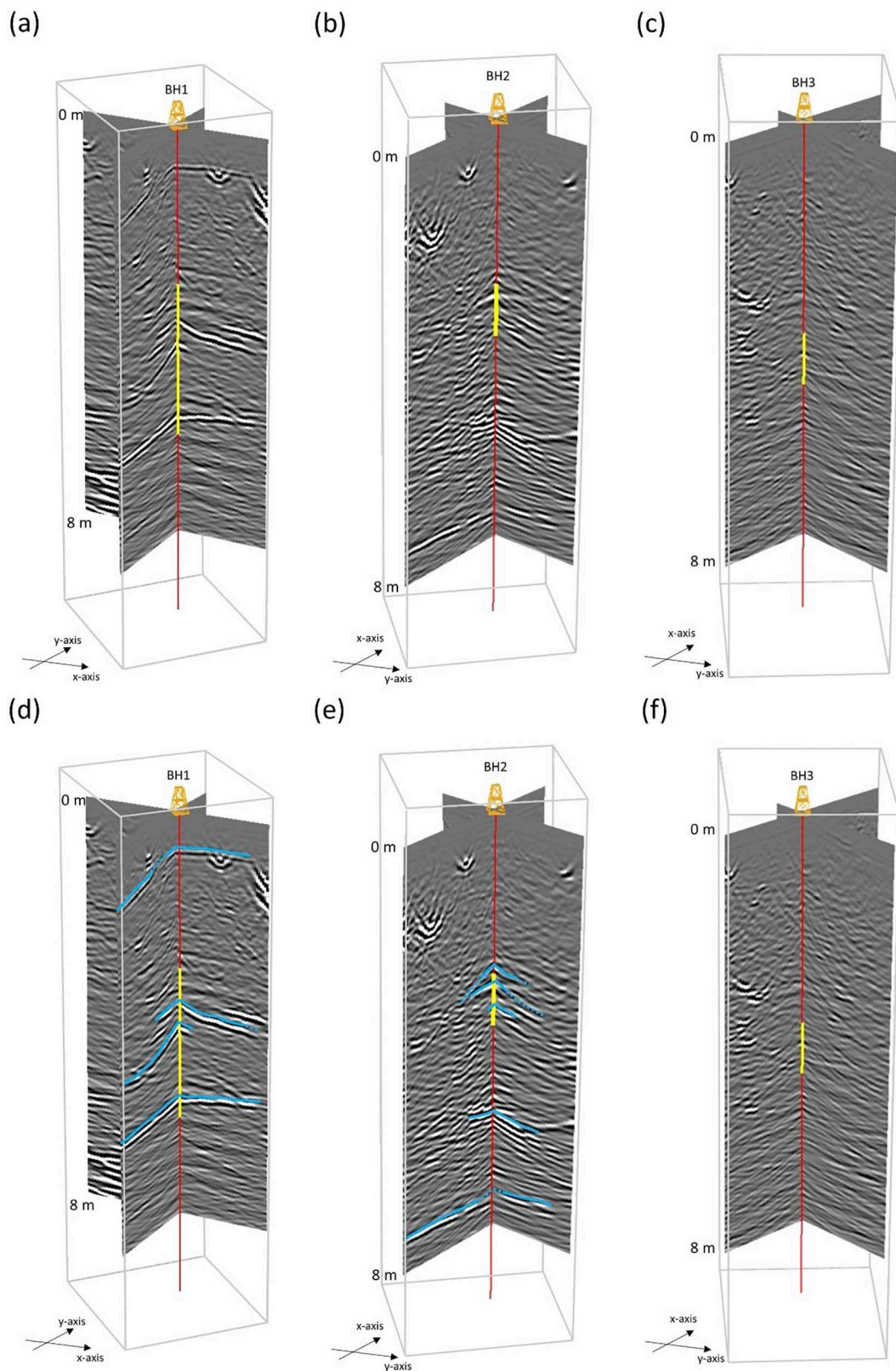


**Fig. 10.** Fence diagrams displaying migrated data (450 MHz) crossing each borehole (BH1, BH2 and BH3). The yellow vertical line segments indicate transmissive 1-m sections as determined by water injection tests, while the red sections induce less flow than the detection limit of 2 mL/min. Transmissive 1-m sections are located between 3 and 6 m depth in BH1, between 3 and 4 m of depth in BH2 and between 4 and 5 m depth in BH3. Uninterpreted GPR sections along BH1 (a), BH2 (b) and BH3 (c) and interpreted GPR sections where strong reflections are represented in full blue lines, while blue dashed lines correspond to the potential extensions of the reflectors along BH1 (d), BH2 (e) and BH3 (f). (For interpretation of the references to colour in this figure legend, the reader is referred to the web version of this article.)

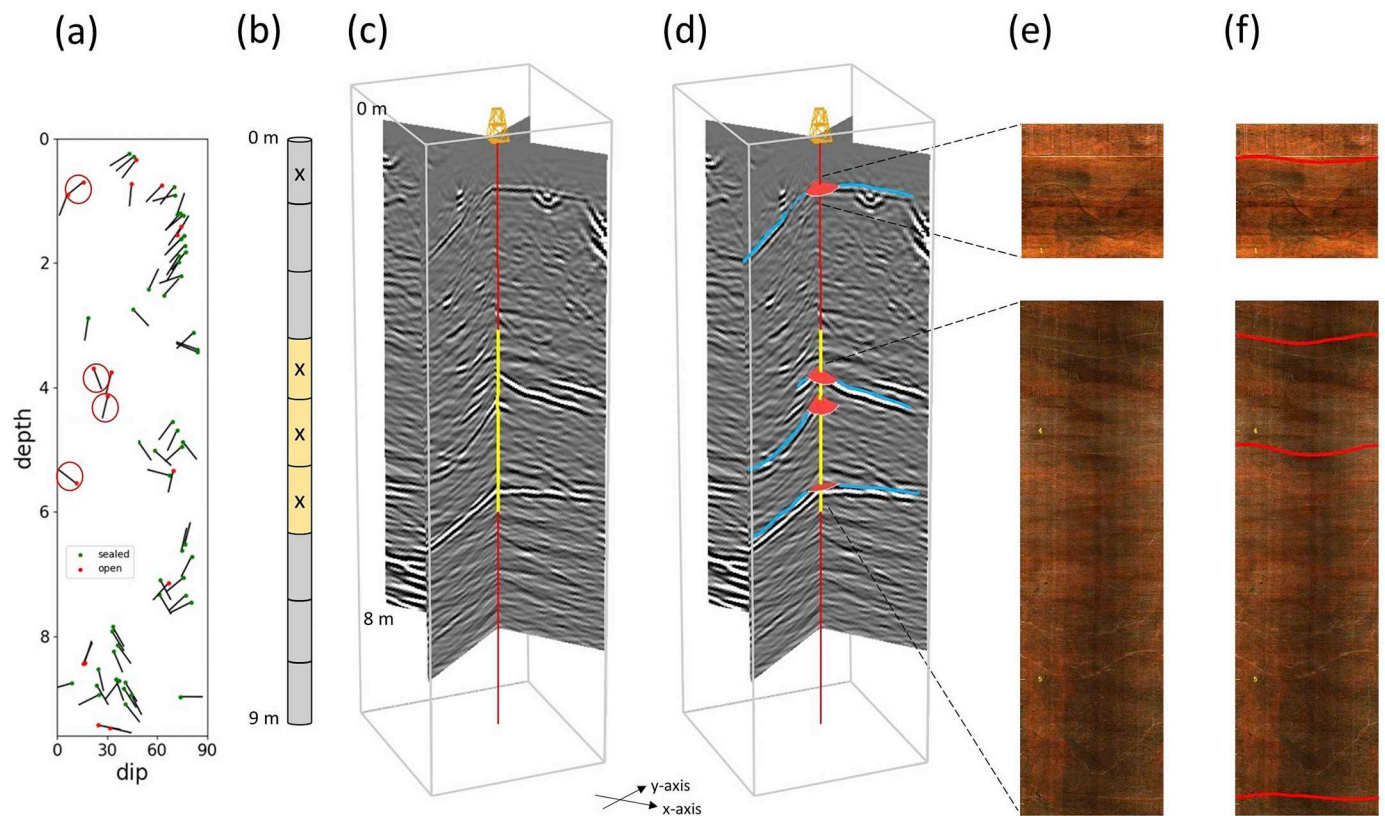


**Fig. 11.** Comparison of core log, hydraulic and GPR data for BH1. (a) Tadpole plot representing the fracture characteristics (depth, orientation and aperture) along the borehole. The circle symbols show the fracture localization in term of depth (y-axis) according to their dip (x-axis). The red and green colors correspond to the open and sealed fractures. The ended black tails represent the direction of the dip, with North (0° and 360°), East (90°), South (180°) and West (270°) being up, right, down and left respectively. The fractures matching by the depth, dip and/or strike with GPR reflectors are encircled in red. (b) Borehole representation with transmissive sections (yellow) and strong reflections (cross in the middle of the sections). Fence diagrams display migrated GPR data (450 MHz) crossing BH1 (c) before and (d) after interpretation. The identified transmissive zones are represented in yellow and fractures logged along the borehole and matching (by depth, strike and/or dip) with strong GPR reflections (blue lines) are symbolized by red disks (open fracture) centered on the borehole. (e) Uninterpreted and (f) interpreted Optical Televiewer images showing the fracture traces on borehole walls. Fractures matching with GPR reflectors are underlined in red lines. Yellow depth scale corresponds to the depth recorded by the Televiewer. (For interpretation of the references to colour in this figure legend, the reader is referred to the web version of this article.)

vertical fractures, highlighting the well-known fact that surface-based GPR is unable to image very steeply dipping fractures.

## 6. Statistical completeness and GPR agreement

The proportion of existing fractures that are identified by GPR likely depends on the fracture size, orientation and filling content. In order to estimate this ratio, we derived the 3-D orientation and size distribution of fractures from the fracture traces observed in the surrounding tunnel walls. The following sections describe the methodology used and compare the density of GPR-observed fractures to the expected values derived from this 3-D density distribution.

### 6.1. Tunnel data (size and orientation distributions of fracture traces)

In addition to the tunnel (TAS04) in which the GPR experiment was carried out, we also used information from two parallel (TAS05 and

TASN) and one perpendicular tunnel (TASP). A total of 3513 fracture traces have been observed on tunnel walls and stored in the SKB database together with their fracture characteristics: trace length, orientation (dip and strike), aperture, mineral filling and fracture shape. The trace length density distribution per unit surface is shown in Fig. 14. It exhibits two different scaling behaviors above and below 3.6 m even after removing censoring and edge biases (Laslett, 1982), that is, fracture traces smaller than 1 m and larger than 8.6 m. The observed trend is fitted by a power law with a scaling exponent of  $-2$  for small traces and  $-3$  for large ones. This two-power-law trace size distribution model is consistent with the analysis of outcrop maps in the same area (Davy et al., 2010).

The stereonet of fracture trace orientation poles (i.e., one pole per fracture) is given in Fig. 15a. It shows three main orientation poles: two vertical ones trending NW and NE, and one horizontal. The comparison of the fracture trace orientation with those of the GPR fractures is described in section 6.3.

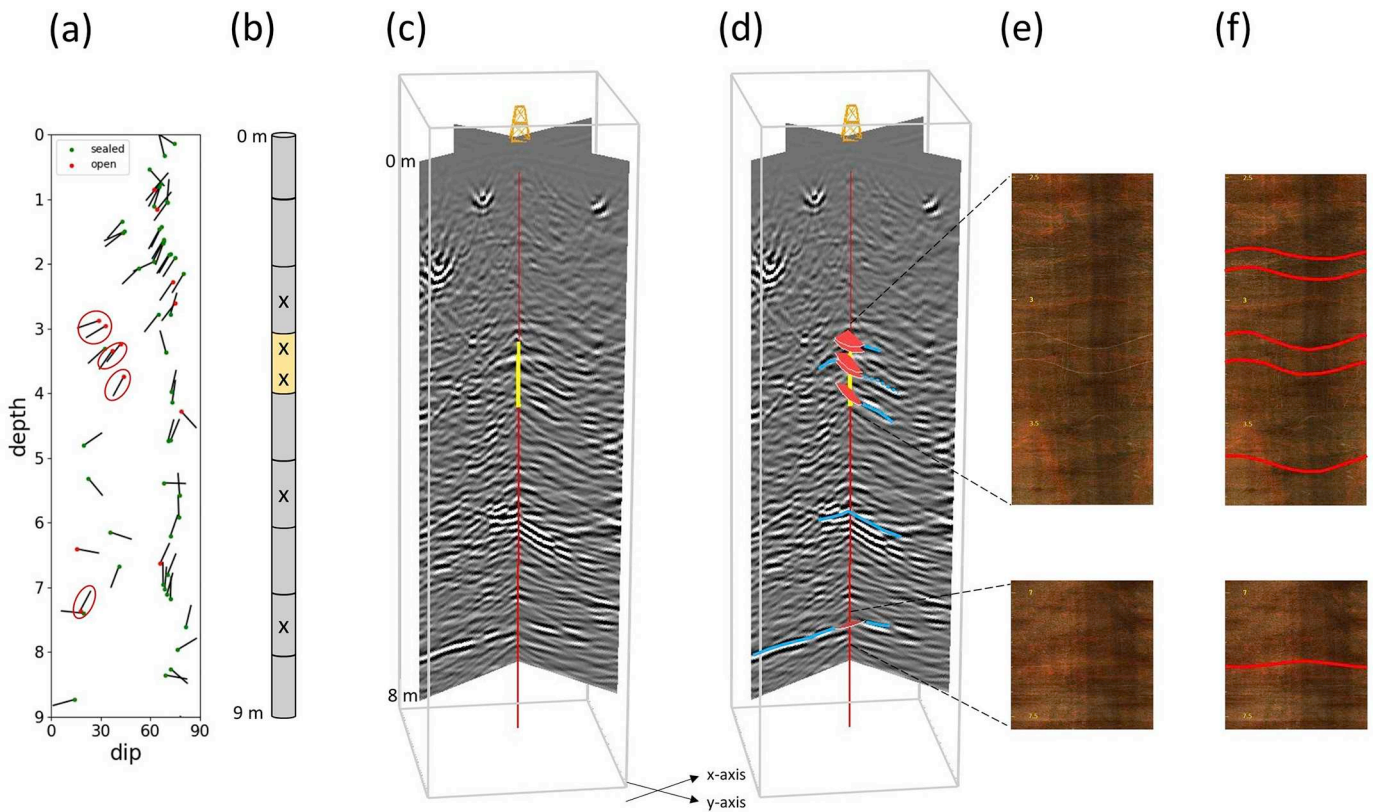


**Fig. 12.** Comparison of core log, hydraulic and GPR data for BH2. (a) Tadpole representing the fracture characteristics (depth, orientation and aperture) along the borehole. The circle symbols show the fracture localization in term of depth (y-axis) according to their dip (x-axis). The red and green colors correspond to the open and sealed fractures. The ended black tails represent the direction of the dip, with North (0° and 360°), East (90°), South (180°) and West (270°) being up, right, down and left respectively. The fractures matching by the depth, dip and/or strike with GPR reflectors are encircled in red. (b) Borehole representation with transmissive sections (yellow) and strong reflections (cross in the middle of the sections) Fence diagrams display migrated GPR data (450 MHz) crossing BH2 (c) before and (d) after interpretation. The identified transmissive zones are represented in yellow and fractures logged along the borehole and matching (by depth, strike and/or dip) with strong GPR reflections (blue lines) are symbolized by red disks (open fracture) centered on the borehole. (e) Uninterpreted and (f) interpreted Optical Televiewer images showing the fracture traces on borehole walls. Fractures matching with GPR reflectors are underlined in red lines. Yellow depth scale corresponds to the depth recorded by the Televiewer. (For interpretation of the references to colour in this figure legend, the reader is referred to the web version of this article.)

### 6.2. 3-D statistical model

The 3-D statistical model is calculated by assuming disk-shaped fractures and that the orientation distribution is similar for all fracture sizes in the target range (1–8 m). The statistical model is based on trace size distribution and orientation developed in section 6.1 and its consistency has been checked on three realizations.

The 3-D distribution parameters (density and power law exponent terms) are calculated according to the stereological rules described by Piggott (1997). These rules were initially applied for an infinite surface with fractures having uniform orientation. Nevertheless, they have been tested by several simulations for non-uniform fractures sampled on cylindrical tunnels and it shows that Piggott's rules can be applied for fractures sampled on tunnel walls (Appendix A). For a power law and assuming that fractures are disk shaped, the relation is:

$$\alpha_{3D} = \alpha_{2D} + 1, \tag{3}$$

$$\alpha_{3D} = \alpha_{2D} \sqrt{\pi} \frac{\Gamma\left(\frac{2 + \alpha_{2D}}{2}\right)}{\Gamma\left(\frac{1 + \alpha_{2D}}{2}\right)}, \tag{4}$$

where  $\alpha_{2D}$  and  $\alpha_{3D}$  are the 2-D and 3-D exponents of fracture traces and sizes, respectively, and  $\alpha_{2D}$  and  $\alpha_{3D}$  are the density terms in 2-D and 3-D, respectively. The calculated 3-D density parameters are  $\alpha_{3D} = 1.6$  and  $\alpha_{3D} = 3$  for fracture sizes between 1 m and 4.2 m and  $\alpha_{3D} = 6.8$  and  $\alpha_{3D} = 4$  for fracture lengths above 4.2 m.

The fracture orientations are calculated from the occurrence of fracture traces by applying a weighting factor equal to the angular correction of Mauldon and Mauldon (1997) for a cylindrical tunnel and fracture sizes smaller than the tunnel diameter:

$$\omega(\theta) = \sqrt{\frac{2}{1 + \cos^2(\theta)}}, \tag{5}$$

where  $\theta$  is the angle between the fracture pole and the tunnel direction.

We verify from direct simulations (i.e., calculating fracture traces from a 3-D fracture network generated with the size and orientation distribution deduced from Eqs. (3), (4) and (5)) that the model is consistent with data, and consequently that:

- The cylindrical-shape assumption is valid even if tunnels have more complex shapes;

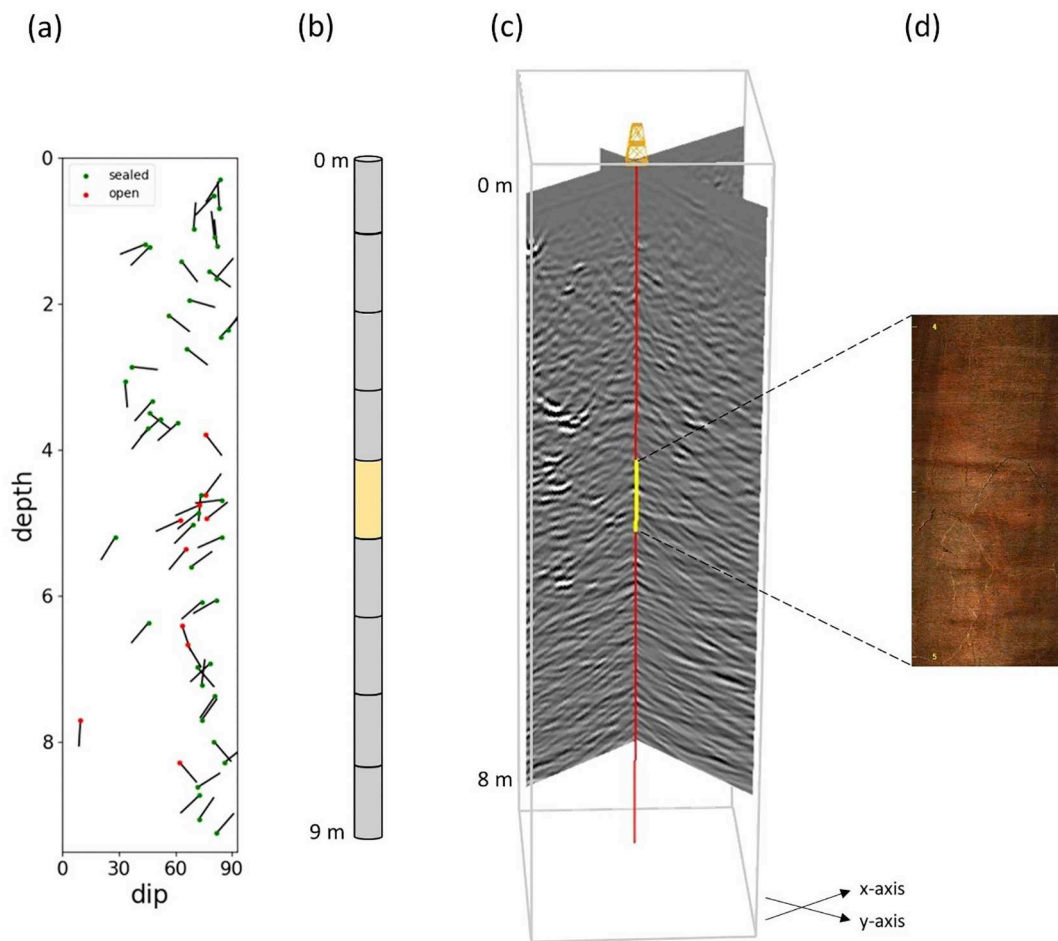


**Fig. 13.** Comparison of core log, hydraulic and GPR data for BH3. (a) Tadpole plot representing the fracture characteristics (depth, orientation and aperture) along the borehole. The circle symbols show the fracture localization in term of depth (y-axis) according to their dip (x-axis). The red and green colors correspond to the open and sealed fractures. The ended black tails represent the direction of the dip, with North (0° and 360°), East (90°), South (180°) and West (270°) being up, right, down and left respectively. (b) Borehole representation with transmissive sections (yellow). No strong GPR reflections are listed. Fence diagrams display migrated GPR data (450 MHz) crossing BH3 (c). The identified transmissive zone is represented in yellow. No reflector is seen along the BH3 and no matching could be done. (d) Optical Televiever images showing the transmissive zone composed mostly by open fractures with dips > 60°. Yellow depth scale corresponds to the depth recorded by the Televiever. (For interpretation of the references to colour in this figure legend, the reader is referred to the web version of this article.)

**Table 3**

Matching criteria based on the depth, strike and dip comparison between GPR reflectors (R) and core logged fractures (F). A maximum threshold was defined: 0.3 m for depth, 15° for dip and 60° for strike. The matching criteria is validated when the gap (calculated by subtracting values from R and F) is below the threshold (v). Any values above this threshold are rejected (x).

Borehole ID	Depth (m)			Strike (° N)			Dip (°)			Matching criteria		
	R	F	Gap	R	F	Gap	R	F	Gap	Depth	Strike	Dip
BH1	0.7	0.7	0	166	141	25	10	16	6	v	v	v
	3.7	3.7	0	123	69	54	22	22	0	v	v	v
	4.2	4.1	0.1	141	104	37	24	30	6	v	v	v
	5.6	5.5	0.1	188	218	30	8	11	3	v	v	v
BH2	2.9	2.9	0	181	161	20	27	29	2	v	v	v
		3.0	0.1		149	32		33	6	v	v	v
	3.2	3.2	0	117	128	11	6	42	36	v	v	x
		3.3	0.1		125	8		37	31	v	v	x
	3.7	3.7	0	84	119	35	30	44	14	v	v	v
	5.7	/	/	102	/	/	18	/	/	x	x	x
	7.4	7.4	0	329	298	30	11	18	7	v	v	v

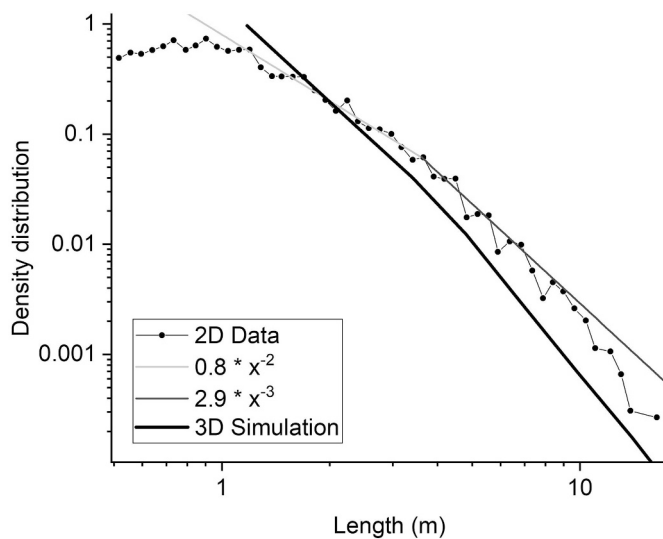


**Fig. 14.** Trace and fracture length density distribution per unit surface and volume, respectively. The trace length distribution is represented by black dots corresponding to the number of fracture traces observed on tunnel walls normalized by tunnel surfaces (y-axis), in size ranges using logarithmic binning. The fits of the trend are represented by light and dark gray curves for fractures smaller and larger than 3.6 m, following a power law. The corresponding 3-D distribution (black curve) was calculated from stereological rules (Piggott, 1997) applied to trace data.

- The two-power-law model is required to honor the observed trace distribution. We check that the large-scale power-law regime is distinct from the finite-size effect due to the tunnel diameter.

Considering the density and orientation characteristics, the 3-D distribution of fracture sizes is then calculated (Fig. 14), which gives the number of fractures per unit area, per unit pole angle and per unit volume.

### 6.3. Comparison with GPR fracture distribution

The comparison with the orientation distribution deduced from fracture traces shows that the GPR fracture orientation (picked from all frequencies) corresponds to the sub-horizontal poles (dip <math>< 35^\circ</math>) of the fracture traces (Fig. 15b). Since the GPR has imaged the fractures with area from 1 to  $10\text{m}^2$  and dip less than  $35^\circ$ , we compared the same fracture population in the 3-D statistical model. We first estimated the detection capacity of GPR by dividing the observed density (total surface by unit of volume per dip range) with the 3-D modeled density calculated in the section 6.2 (Fig. 16a). The observed fluctuations between  $0$  and  $20\text{--}25^\circ$  may be due to the limited number GPR fractures, but there is a clear cut-off of detection above  $25^\circ$  even if some GPR fractures are detected between  $25$  and  $35^\circ$ . On average, 5.5% of the fractures with area of  $1\text{--}10\text{m}^2$  were detected by GPR. This result is a direct consequence of the geometry of the GPR antenna, where the surface-based acquisition favors the imaging of sub-horizontal fractures. This ratio rises to 42% for any type of fracture apertures (opened or sealed) when considering fractures dipping less than  $25^\circ$ . The ratio of

open fractures in the borehole data (Table 4) is 53% for fractures dipping less than  $25^\circ$ . Assuming that this is also the ratio for  $1\text{--}10\text{m}^2$  fractures, we find that the GPR method is likely imaging 80% of the open fractures with dip <math>< 25^\circ</math>.

According to the GPR fracture dip cut-off, the area distribution of GPR fractures have been calculated (e.g., number of fractures per unit area and unit volume) for all fractures dipping less than  $25^\circ$  (Fig. 16b). In a log-log plot, it appears to follow the same power-law trend as the 3-D modeled area distribution. The dashed line represents the plot of the modeled distribution area for fractures in the same dip range considering that 80% of the actual fractures are detected. A remarkable result is that it fits well the GPR data within the data uncertainties (Fig. 16b). The fact that the fracture area distribution in the range  $1\text{--}10\text{m}^2$  is similar to the 3-D area distribution modeled by extrapolating the tunnel fracture traces means that the GPR is able to image the fractures in proportion to the length distribution trend (no size selection). This is a promising result, but it does not offer a definite conclusion because of the small number of GPR fractures, and because of the uncertainty on the modeled distribution due to the assumptions used.

## 7. Conclusions and perspectives

The purpose of this work was to assess the ability of the GPR method to image fractures with sub-millimetric aperture in a very low permeable crystalline rock. To do so, we performed surface-based measurements in a tunnel situated at 410 m depth. GPR profiles were measured in a 3-D configuration ( $3.4\text{m} \times 19\text{m}$ ) using three frequencies (160, 450 and 750 MHz). A total of 17 sub-horizontal reflections were manually picked from the 3-D acquisition block, whose minimum and maximum length were 0.8 m and 5 m, respectively. To define the nature of these reflections, three boreholes (BH1-BH3; 9–9.5 m deep) were drilled. A very good correlation in terms of depth and orientation between the GPR reflections crossing BH1 and BH2 and the open transmissive fractures dipping <math>< 35^\circ</math> located in boreholes was established. The lack of reflections along BH3 is explained by the sub-vertical orientation of the fractures crossing the borehole.

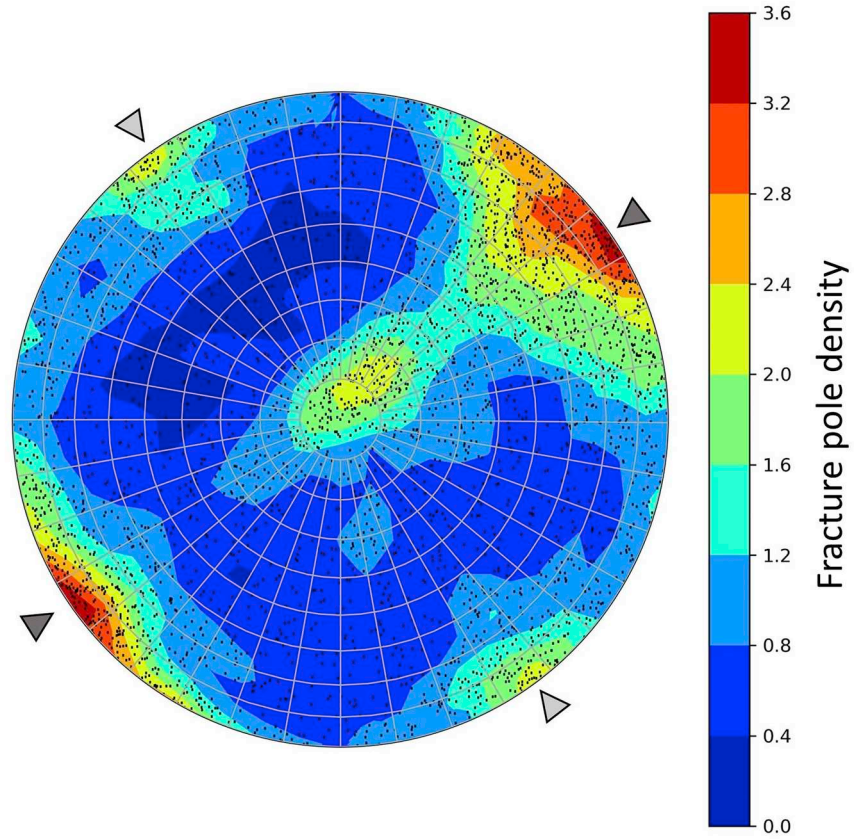
We derived a 3-D statistical fracture density model from fracture traces observed on surrounding tunnels walls. This density model predicts the expected number of fractures in the domain for given orientations and sizes, thereby, enabling comparison with the distribution of GPR fractures. The comparison is made for fracture areas in the range  $1\text{--}10\text{m}^2$ , which contains most of the GPR fractures detected by 160, 450 and 750 MHz antennas. The percentage of fractures detected by GPR is:

- 5.5% of all the observed fractures regardless of orientation or if they are open or sealed;
- 42% of the fractures dipping less than  $25^\circ$ ;
- 80% of open fractures dipping less than  $25^\circ$ .

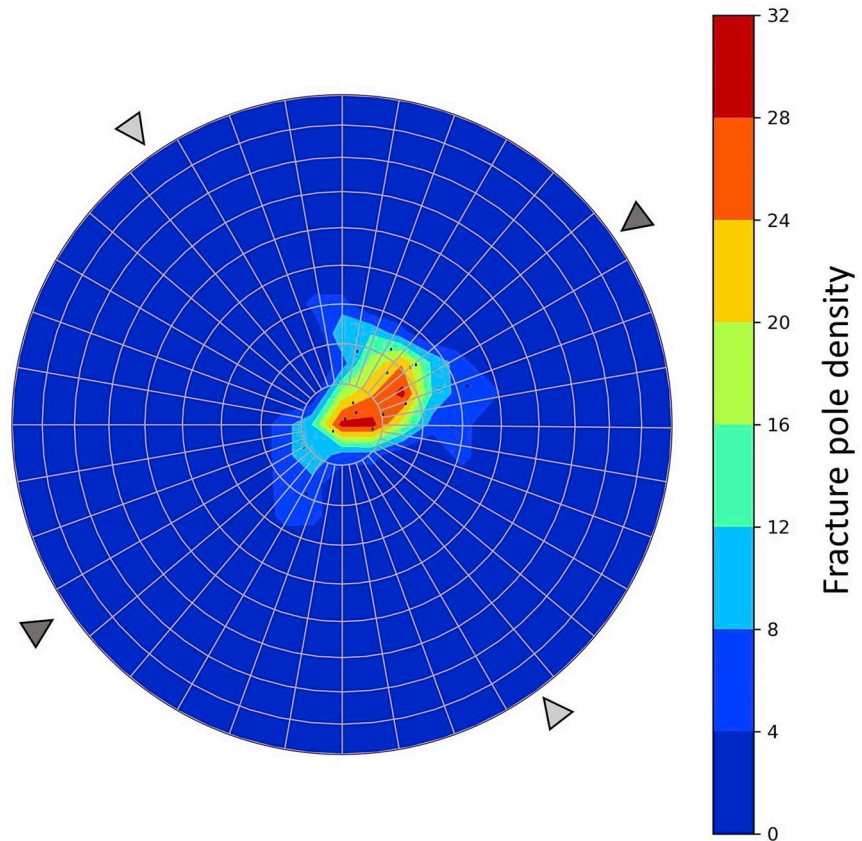
In addition, the dependency with size of the GPR fracture density distribution is similar to the real fracture density distribution. Both size distributions fit perfectly if one considers the sub-network of open fractures dipping less than  $25^\circ$ . This result indicates that there is no size selection in the range of  $1\text{--}10\text{m}^2$  by GPR imaging (the ratio between the fracture size is conserved).

We conclude that GPR imaging can be very efficient to detect open

(a)



(b)



(caption on next page)

**Fig. 15.** Stereonet representation (equal area projection) showing fracture orientation poles (black dots). The strike is indicated around the circle, with North (0° and 360°), East (90°), South (180°) and West (270°) being up, right, down and left respectively while the dip is seen from the middle (0°) to the edge of the stereonet (90°). The density colour scale represents the fracture density distribution according to orientation units, explaining higher density values for GPR fracture orientations. Tunnel orientations are represented by dark (TASP) and light (TAS04, TAS05 and TASN) gray triangles. (a) Representation of the fracture trace orientation poles (3513) showing two vertical trending (NW and NE) following the tunnel directions and one horizontal (middle of stereonet), (b) fracture pole orientations imaged by GPR (17) showing a horizontal trend of the fractures.

sub-horizontal fractures with sub-millimeter aperture. The resolution of the present statistical analysis is limited to ~1 m, mainly because of the cut-off of fracture traces during the tunnel mapping, which constrained the comparative analysis to this minimum fracture size. The largest fractures and the fracture orientations are limited by the geometry of the acquisition setup. Further work is planned to use time-lapse GPR imaging for tracing solute transport in the fracture network similarly to Dorn et al. (2011b) and Shakas et al. (2016). The main objective of this experiment is to hydraulically characterize the fracture media and identify the potential conduit for flows.

**Table 4**

Ratio of GPR detection according to fracture parameters: dip and aperture. Analysis is focused on the open fractures intersecting the boreholes (BH1 to BH3), dipping less than 25°.

Fracture parameters		Borehole fractures	GPR
Dip	Aperture	Number	Imaging probability
0–90°	open + sealed	188	5.5%
< 25°	open + sealed	19	41.6%
< 25°	open	10 (52.6%)	79.1%

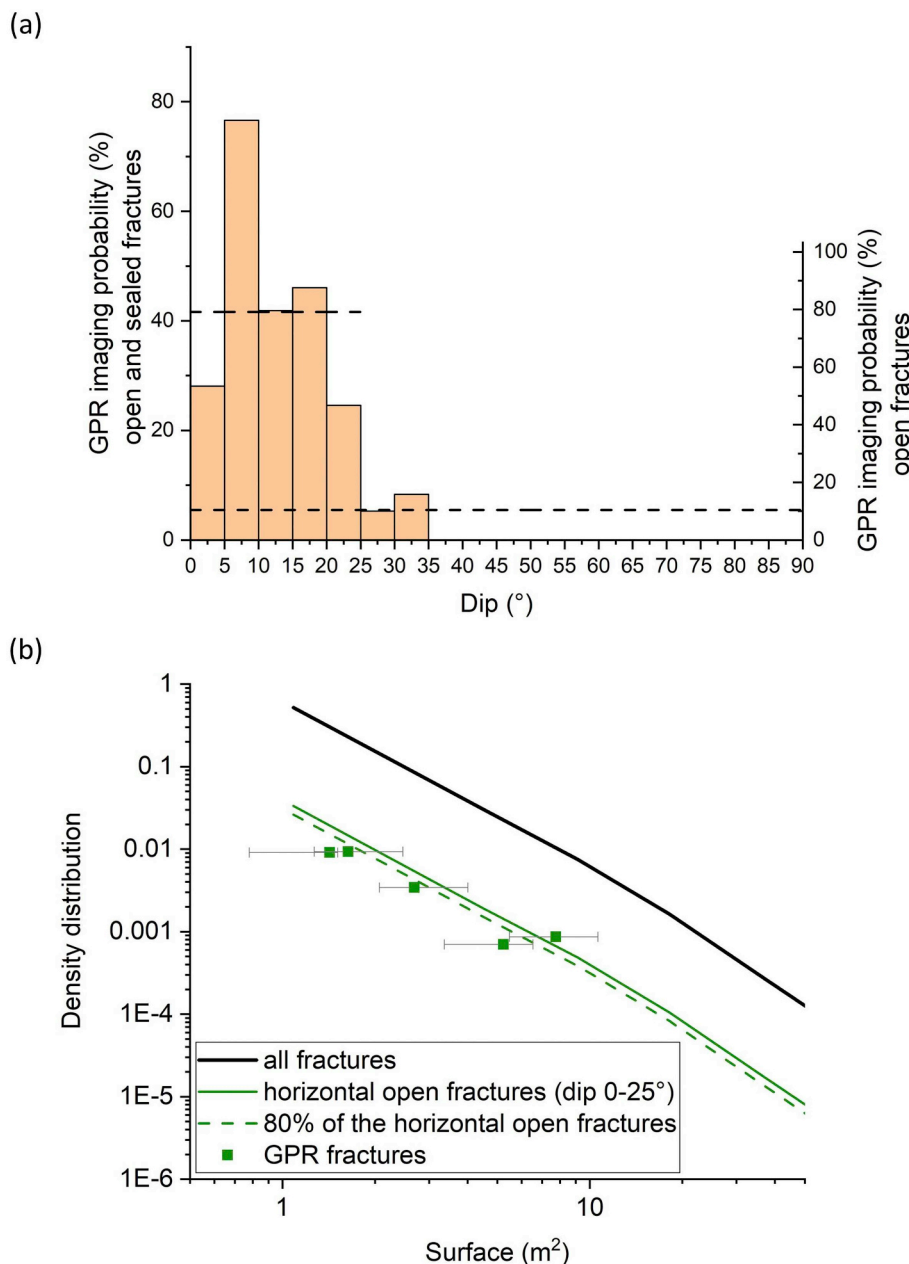


**Fig. 16.** (a) GPR detection capacity for open and sealed (left y-axis) and open (right y-axis) fractures having an area between 1 and 10 m<sup>2</sup> according to the dip (x-axis). The detectability cut-offs are represented by black dashed curves (b) Comparison of the modeled 3-D density and GPR density distribution. The area distribution of GPR fractures (y-axis) included in area ranges using an overlapping logarithmic binning (x-axis). Gray bars represent the data uncertainties corresponding to bin limits. The 3-D density model deduced from fracture traces comprised in dip ranges of [0–90°], [0–25°] and [0–25°]\*80% are represented by black curve, green curve and dashed green curve, respectively. (For interpretation of the references to colour in this figure legend, the reader is referred to the web version of this article.)

**Declaration of Competing Interest**

The authors declare that they have no known competing financial interests or personal relationships that could have appeared to influence the work reported in this paper.

**Acknowledgements**

This research is part of the ENIGMA ITN project that has received funding from the European Union's Horizon 2020 research and innovation programme under the Marie Skłodowska-Curie Grant Agreement No 722028. We thank SKB for its great support, particularly

Lars Andersson, Patrik Vidstrand and Siren Bortelid Robertsson. The GPR data and core log data are stored in the Sicada database and can be made available after an official request to SKB. We also thank Geosigma, particularly Peter Andersson and Johanna Ragvald, for their quality fieldwork and detailed report and Christian Le Carlier De Veslud from Géosciences Rennes for his valuable help to use Paradigm GOCAD™. Two constructive reviews from anonymous reviewers are greatly appreciated. Finally, this research is also supported by the French National Observatory H+. The GPR data in WGS84 coordinates are available (after requesting login ID and password through <http://hplus.ore.fr/en/database/acces-database>) at <http://hplus.ore.fr/en/molron-et-al-2020-eg-data>.

**Piggott stereology tested on non-uniform orientation and cylindrical outcrops**

Piggott (1997) derived the stereological rules that give the 3-D size distribution of uniformly-oriented disk fractures from a power-law size distribution of fracture traces measured on an infinite plane:

$$a_{3D} = a_{2D} + 1,$$

$$\alpha_{3D} = \alpha_{2D} \sqrt{\pi} \frac{\Gamma\left(\frac{2 + a_{2D}}{2}\right)}{\Gamma\left(\frac{1 + a_{2D}}{2}\right)},$$

with  $a_{2D}$  and  $a_{3D}$  being the 2-D and 3-D exponents of fracture traces and sizes, respectively, and  $\alpha_{2D}$  and  $\alpha_{3D}$  being the density terms in 2-D and 3-D, respectively.

Here we test whether similar rules can be applied to a finite cylindrical tunnel. For this, we run 3-D simulations where fracture networks are generated with a power-law size distribution and non-uniform orientations, and fracture traces are identified on the wall of a cylindrical tunnel. We then calculate the trace size distributions, fit them with a power law, and compare the fit with Piggott's formulae (Fig. A.1). The ratio between the power-law fits and Piggott's formulae reaches 1.5, 1.2, 1.1 and 1 for  $a_{2D}$  of 2.0 (1,652,131 fractures and 2834 fracture traces), 2.5 (1,156,665 fractures and 1479 fractures traces), 3.0 (924,152 fractures and 1007 fracture traces) and 3.5 (786,477 fractures and 791 traces) respectively. To support our analysis, we compare the fracture trace size distribution observed on tunnel walls with our statistical model generated with a double power-law size distribution and orientation bootstrapped from data (Fig. A.2).

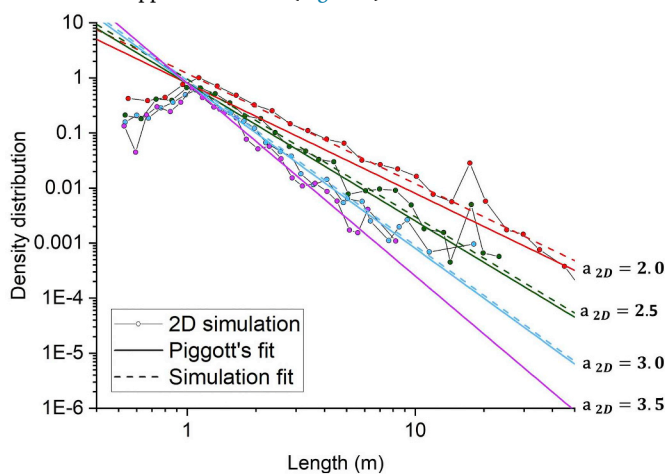


**Fig. A.1.** Trace length density distributions (lines with circles) deduced from 3D simulations ran according to a single power-law and different exponents ( $a_{2D}$  terms). Solid lines are the expected fits calculated by stereological rules and dashed lines are the real fits.

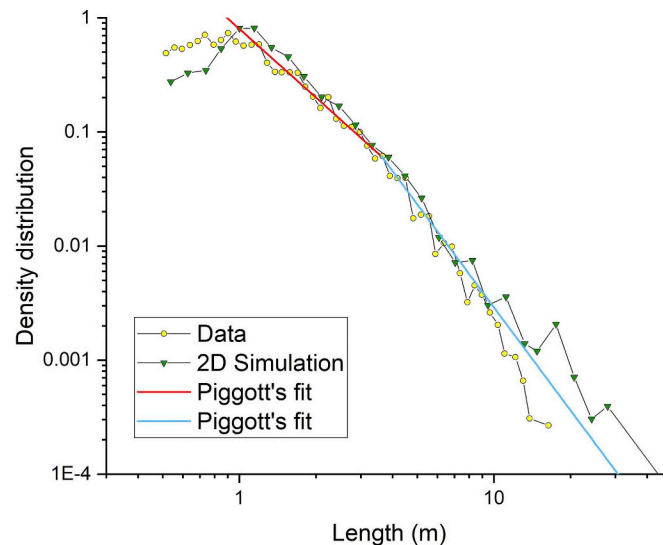


**Fig. A.2.** Comparison of fracture trace density distribution between the data (yellow) and the statistical model (green) using Piggott's stereological rules. The red and blue curves are the fits for fractures smaller and larger than 3.6 m, respectively. (For interpretation of the references to colour in this figure legend, the reader is referred to the web version of this article.)

## References

- Andersson, J., Dverstorp, B., 1987. Conditional simulations of fluid flow in three-dimensional networks of discrete fractures. *Water Resour. Res.* 23 (10), 1876–1886. <https://doi.org/10.1029/WR023i010p01876>.
- Andersson, P., Ragvald, J., 2019. ENIGMA - Poject. GPR monitoring of fractures at Äspö HRL, Results of field investigations in TAS04 at Äspö HRL, (P-19-17). Retrieved from Stockholm, Sweden.
- Annan, P., 2003. *Ground Penetrating Radar Principles, Procedures and Applications*. Retrieved from Mississauga, ON, Canada.
- Baek, S.H., Kim, S.S., Kwon, J.S., Um, E.S., 2017. Ground penetrating radar for fracture mapping in underground hazardous waste disposal sites: a case study from an underground research tunnel, South Korea. *J. Appl. Geophys.* 141, 24–33. <https://doi.org/10.1016/j.jappgeo.2017.03.017>.
- Becker, M.W., Shapiro, A.M., 2000. Tracer transport in fractured crystalline rock: evidence of nondiffusive breakthrough tailing. *Water Resour. Res.* 36 (7), 1677–1686.
- Becker, M., Tsofilas, G., 2010. Comparing flux-averaged and resident concentration in a fractured bedrock using ground penetrating radar. *Water Resour. Res.* 46 (9). <https://doi.org/10.1029/2009WR008260>.
- Bradford, J.H., Deeds, J.C., 2006. Ground-penetrating radar theory and application of thin-bed offset-dependent reflectivity. *Geophysics* 71 (3), K47–K57. <https://doi.org/10.1190/1.2194524>.
- Cosma, C., Olsson, O., Keskinen, J., Heikkinen, P., 2001. Seismic characterization of fracturing at the Äspö Hard Rock Laboratory, Sweden, from the kilometer scale to the meter scale. *Int. J. Rock Mech. Min.* 38 (6), 859–865. [https://doi.org/10.1016/S1365-1609\(01\)00051-X](https://doi.org/10.1016/S1365-1609(01)00051-X).
- CREWES, 1988. CREWES Matlab Toolbox. <https://www.crewes.org/ResearchLinks/FreeSoftware/> accessed 20 November 2017.
- Davis, J.L., Annan, A.P., 1989. Ground-Penetrating Radar for High-resolution mapping of soil and rock stratigraphy. *Geophys. Prospect.* 37 (5), 531–551. <https://doi.org/10.1111/j.1365-2478.1989.tb02221.x>.
- Davy, P., Le Goc, R., Darcel, C., Bour, O., De Dreuzy, J.R., Munier, R., 2010. A likely universal model of fracture scaling and its consequence for crustal hydromechanics. *J. Geophys. Res.: Solid Earth* 115, B10411. <https://doi.org/10.1029/2009JB007043>.
- Davy, P., Darcel, C., Le Goc, R., Mas Ivars, D., 2018a. Elastic properties of fractured rock masses with frictional properties and power law fracture size distributions. *J. Geophys. Res. Solid Earth* 123 (8), 6521–6539. <https://doi.org/10.1029/2017JB015329>.
- Davy, P., Darcel, C., Le Goc, R., Munier, R., Selroos, J.-O., Mas Ivars, D., 2018b. DFN, why, how and what for, concepts, theories and issues. In: Paper presented at the 2nd International Discrete Fracture Network Engineering Conference.
- Day-Lewis, F.D., Lane, J.W., Harris, J.M., Gorelick, S.M., 2003. Time-lapse imaging of saline-tracer transport in fractured rock using difference-attenuation radar tomography. *Water Resour. Res.* 39 (10). <https://doi.org/10.1029/2002wr001722>.
- Day-Lewis, F.D., Slater, L.D., Robinson, J., Johnson, C.D., Terry, N., Werkema, D., 2017. An overview of geophysical technologies appropriate for characterization and monitoring at fractured-rock sites. *J. Environ. Manag.* 204, 709–720.
- Deparis, J., Garambois, S., 2008. On the use of dispersive APVO GPR curves for thin-bed properties estimation: Theory and application to fracture characterization. *Geophysics* 74 (1), J1–J12. <https://doi.org/10.1190/1.3008545>.
- Dorn, C., Linde, N., Doetsch, J., Le Borgne, T., Bour, O., 2011a. Fracture imaging within a granitic rock aquifer using multiple-offset single-hole and cross-hole GPR reflection data. *J. Appl. Geophys.* 78, 123–132. <https://doi.org/10.1016/j.jappgeo.2011.01.010>.
- Dorn, C., Linde, N., Le Borgne, T., Bour, O., Baron, L., 2011b. Single-hole GPR reflection imaging of solute transport in a granitic aquifer. *Geophys. Res. Lett.* 38 (8). <https://doi.org/10.1029/2011gl047152>.
- Dorn, C., Linde, N., Le Borgne, T., Bour, O., Klepikova, M., 2012. Inferring transport characteristics in a fractured rock aquifer by combining single-hole ground-penetrating radar reflection monitoring and tracer test data. *Water Resour. Res.* 48 (11). <https://doi.org/10.1029/2011wr011739>.
- Döse, C., Carlsten, S., 2017. Investigation for identification of potential geological signatures for geophysical objects, (P-11-34). Retrieved from Stockholm, Sweden.
- Ericsson, L., Lehtimäki, R.C., Ittner, T., Hansson, H., Butron, K., Sigurdsson, C., Kinnbom, P., 2015. A demonstration project on controlling and verifying the excavation-damaged zone, (R-14-30). Retrieved from Stockholm, Sweden.
- Ericsson, L., Vidstrand, P., Christiansson, R., Morosini, M., 2018. Comparison Between Blasting and Wire Sawing Regarding Hydraulic Properties of the Excavated Damaged Zone in a Tunnel—Experiences From Crystalline Rock at the Äspö Hard Rock Laboratory, Sweden. In: Paper presented at the 52nd US Rock Mechanics/ Geomechanics Symposium.
- Grasmueck, M., 1996. 3-D ground-penetrating radar applied to fracture imaging in gneiss. *Geophysics* 61 (4), 1050–1064. <https://doi.org/10.1190/1.1444026>.
- Grasmueck, M.W., Ralf, Horstmeyer, Heinrich, 2005a. Full-resolution 3D GPR imaging. *Geophysics* 70 (1).
- Grasmueck, M., Weger, R., Horstmeyer, H., 2005b. Full-resolution 3D GPR imaging. *Geophysics* 70 (1), K12–K19. <https://doi.org/10.1190/1.1852780>.
- Grasmueck, M., Quintà, M.C., Pomar, K., Eberli, G.P., 2013. Diffraction imaging of sub-vertical fractures and karst with full-resolution 3D ground-penetrating radar. *Geophys. Prospect.* 61 (5), 907–918. <https://doi.org/10.1111/1365-2478.12004>.
- Grasmueck, M., Moser, T.J., Pelissier, M.A., Pajchel, J., Pomar, K., 2015. Diffraction signatures of fracture intersections. *Interpretation* 3 (1), SF55–SF68. <https://doi.org/10.1190/INT-2014-0086.1>.
- Grégoire, C., Halleux, L., 2002. Characterization of fractures by GPR in a mining environment. *First Break* 20 (7), 467–471.
- Grégoire, C., Hollender, F., 2004. Discontinuity characterization by the inversion of the spectral content of ground penetrating radar (GPR) reflections—Application of the Jonscher model. *Geophysics* 69 (6), 1414–1424. <https://doi.org/10.1190/1.1836816>.
- Hjerne, C., Ludvigsson, J.E., Harrström, J., Olofsson, C., Gokall-Norman, K., Walger, E., 2013. Äspö Hard Rock Laboratory. Single-hole injection tests in boreholes KA2051A01, KA3007A01 and KJ0050F01, (P-13-24). Retrieved from Stockholm, Sweden.
- Hollender, F., Tillard, S., 1998. Modeling ground-penetrating radar wave propagation and reflection with the Jonscher parameterization. *Geophysics* 63 (6), 1933–1942. <https://doi.org/10.1190/1.1444486>.
- Hollender, F., Tillard, S., Corin, L., 1999. Multifold borehole radar acquisition and processing. *Geophys. Prospect.* 47 (6), 1077–1090. <https://doi.org/10.1046/j.1365-2478.1999.00166.x>.
- Jeannin, M., Garambois, S., Grégoire, C., Jongmans, D., 2006. Multiconfiguration GPR measurements for geometric fracture characterization in limestone cliffs (Alps). *Geophysics* 71 (3), B85–B92. <https://doi.org/10.1190/1.2194526>.
- Jol, H.M., 2008. *Ground Penetrating Radar Theory and Applications*. Elsevier, Amsterdam, The Netherlands.
- Laslett, G.M., 1982. Censoring and Edge Effects in Areal and Line Transect Sampling of

- Rock Joint Traces. *Math. Geol.* 14 (2), 125–140.
- Margrave, G.F., Lamoureux, M.P., 2019. *Numerical Methods of Exploration Seismology: With Algorithms in MATLAB®*. Cambridge University Press.
- Markovaara-Koivisto, M., Hokkanen, T., Huuskonen-Snicker, E., 2014. The effect of fracture aperture and filling material on GPR signal. *B. Eng. Geol. Environ.* 73 (3), 815–823. <https://doi.org/10.1007/s10064-013-0566-4>.
- Mauldon, M., Mauldon, J.G., 1997. Fracture sampling on a cylinder: from scanlines to boreholes and tunnels. *Rock Mech. Rock Engng.* 30 (3), 129–144.
- Moye, D.G., 1967. *Diamond drilling for foundation exploration*. *Inst. Eng. Civil Eng. Trans/Australia/* 9 (1), 95–100.
- Olsson, O., Falk, L., Forslund, O., Lundmark, L., Sandberg, E., 1992. Borehole radar applied to the characterization of hydraulically conductive fracture zones in crystalline rock. *Geophys. Prospect.* 40 (2), 109–142. <https://doi.org/10.1111/j.1365-2478.1992.tb00367.x>.
- Piggott, A.R., 1997. Fractal relations for the diameter and trace length of disc-shaped fractures. *J. Geophys. Res.* 102 (18), 121–125. <https://doi.org/10.1029/97JB01202>.
- Reynolds, J.M., 1997. *An Introduction to Applied and Environmental Geophysics*. John Wiley & Sons, Chichester, England.
- Sassen, D., Everett, M., 2009. 3D polarimetric GPR coherency attributes and full-waveform inversion of transmission data for characterizing fractured rock. *Geophysics* 74 (3), J23–J34. <https://doi.org/10.1190/1.3103253>.
- Selroos, J.O., Walker, D.D., Ström, A., Gylling, B., Follin, S., 2002. Comparison of alternative modelling approaches for groundwater flow in fractured rock. *J. Hydrol.* 257 (1–4), 174–188. [https://doi.org/10.1016/S0022-1694\(01\)00551-0](https://doi.org/10.1016/S0022-1694(01)00551-0).
- Seol, S.J., Kim, J.H., Song, Y., Chung, S.H., 2001. Finding the strike direction of fractures using GPR. *Geophys. Prospect.* 49 (3), 300–308. <https://doi.org/10.1046/j.1365-2478.2001.00262.x>.
- Serzu, M.H., Kozak, E.T., Lodha, G.S., Everitt, R.A., Woodcock, D.R., 2004. Use of borehole radar techniques to characterize fractured granitic bedrock at AECL's Underground Research Laboratory. *J. Appl. Geophys.* 55 (1–2), 137–150. <https://doi.org/10.1016/j.jappgeo.2003.06.012>.
- Shakas, A., Linde, N., 2015. Effective modeling of ground penetrating radar in fractured media using analytic solutions for propagation, thin-bed interaction and dipolar scattering. *J. Appl. Geophys.* 116, 206–214. <https://doi.org/10.1016/j.jappgeo.2015.03.018>.
- Shakas, A., Linde, N., 2017. Apparent apertures from ground penetrating radar data and their relation to heterogeneous aperture fields. *Geophys. J. Int.* 209 (3), 1418–1430. <https://doi.org/10.1093/gji/ggx100>.
- Shakas, A., Linde, N., Baron, L., Bochet, O., Bour, O., Le Borgne, T., 2016. Hydrogeophysical characterization of transport processes in fractured rock by combining push-pull and single-hole ground penetrating radar experiments. *Water Resour. Res.* 52 (2), 938–953. <https://doi.org/10.1002/2015WR017837>.
- SKB, 2016. *Åspö Hard Rock Laboratory - Annual Report 2015, (TR-16-10)*. Retrieved from Stockholm, Sweden.
- Tsofiias, G.P., Becker, M.W., 2008. Ground-penetrating-radar response to fracture-fluid salinity: why lower frequencies are favorable for resolving salinity changes. *Geophysics* 73 (5), J25–J30. <https://doi.org/10.1190/1.2957893>.
- Tsofiias, G.P., Hoch, A., 2006. Investigating multi-polarization GPR wave transmission through thin layers: Implications for vertical fracture characterization. *Geophys. Res. Lett.* 33 (20). <https://doi.org/10.1029/2006gl027788>.
- Tsofiias, G.P., Halihan, T., Sharp, J.M., 2001. Monitoring pumping test response in a fractured aquifer using ground-penetrating radar. *Water Resour. Res.* 37 (5), 1221–1229. <https://doi.org/10.1029/2000wr900297>.